Electrochemical Analysis of Gold Nanoparticles Multifunctionalised with Cytochrome c and a Zinc Porphyrin

Jordan C. Potts[a], Akhil Jain[b], David B. Amabilino[c], Lluïsa Pérez-García[a,d,e] and Frankie J. Rawson[b]*

[a] Division of Advanced Materials and Healthcare Technologies, School of Pharmacy, University of Nottingham, Nottingham NG7 2RD, UK

[b] Bioelectronics Laboratory, Division of Regenerative Medicine and Cellular Therapies, School of Pharmacy, University of Nottingham, Biodiscovery Institute, Nottingham NG7 2RD, UK

[c] Institut de Ciència de Materials de Barcelona (ICMAB), CSIC, Carrer dels Til·lers, Campus Universitari, 08193 Cerdanyola del Vallès, Catalunya, Spain

[d] Departament de Farmacologia, Toxicologia i Química Terapèutica, Facultat de Farmàcia i Ciències de l'Alimentació, Universitat de Barcelona, 08028 Barcelona, Catalunya, Spain

[e] Institut de Nanociència i Nanotecnologia UB (IN2UB), Universitat de Barcelona, 08028 Barcelona, Catalunya, Spain

Abstract

Cytochrome c (Cyt c), known for its functional redox capabilities, plays a pivotal role in biological processes such as the electron transport chain and apoptosis. However, understanding how different conjugation strategies impact its structural and redox characteristics is limited. To fill this gap, we investigated the effects of conjugating Cyt c and a zinc(II) porphyrin (Zn Porph) to gold nanoparticles (AuNPs). We used circular dichroism (CD) spectroscopy to detect structural conformational changes in Cyt c upon conjugation and time-of-flight secondary ion mass spectrometry (TOF-SIMS) to identify protein orientation. Cyt c was predicted to have different orientations depending on the size of AuNPs and methods used to conjugate the protein, it was hypothesised that the orientation of Cyt

1

c may influence the redox properties of the protein. The electrochemical properties of Cyt *c* were assessed using cyclic voltammetry (CV) and differential pulse voltammetry (DPV). We used DPV-based to determine the heterogeneous rate constant (k^0). The results show a lower k^0 for conjugated Cyt *c* than free Cyt *c*, likely due to structural changes in the protein. The spatial orientation of Cyt *c* had minimal influence on k^0, while ligand density and AuNP size had an effect. The k^0 value of Zn Porph did not decrease on conjugation. Despite these changes, Cyt *c* and Zn Porph maintained their electrochemical capabilities after conjugation.

---

1. Introduction

Cytochrome c (Cyt c), a 12.3 kDa protein, is a focus of research interest due to its unique redox properties [1]. Located at the inner mitochondrial membrane, Cyt c's redox capabilities originate from the iron contained within the central heme moiety, which is capable of existing in Fe^{2+} or Fe^{3+} states, underpinning its primary roles in electron transport and apoptosis [2, 3]. The functionality of such redox proteins extends to diverse sectors, including but not limited to their deployment as biocatalysts, their contribution to biofuel development, their integration into biosensor technologies, their potential in therapeutic interventions, and their application in genetic engineering endeavours. As such, their unique characteristics provoke an intense interest in their exploration and utilisation within the scientific community [4-8].

The employment of redox proteins, such as Cyt c, frequently necessitates immobilisation onto a material substrate. Nanomaterials, due to their extensive potential for applications across diverse fields, several of which intersect with those of Cyt c, are increasingly drawing the attention of the scientific community. Thus, the incidence of Cyt c immobilisation on nanomaterials is not an infrequent activity [9-12]. However, while immobilisation is often reported, there is a discernible lack of discussion surrounding the potential implications that this environment may have on the redox capabilities of Cyt c. It is crucial to investigate this domain, as alterations in redox functionality could critically affect the protein's applicability in various use cases.

Previous research has shown that there are multiple factors in redox protein immobilisation that could influence the redox ability and, therefore, function. Gold nanoparticles (AuNPs) are a

material often used as an immobilisation platform for Cyt *c* to exploit its ability to induce apoptosis or use as a biosensor due to their biocompatibility and unique optical properties [10, 11, 13-16]. A previous study by Romanovskaia et al. found that smaller AuNPs had stronger electrochemical interactions when oxidising with L-cysteine (a thiol-containing amino acids), possibly due to the formation of agglomerates [17], suggesting that the redox ability of a protein like Cyt *c* could be influenced by the size of the material it is immobilised upon. Ligand exchange is a common way that the functionality of AuNPs can be modulated and is often required for the immobilisation of a protein like Cyt *c*. Ligand exchange produces three factors that could influence the redox ability of Cyt *c*, the distance between the surface of the material, the position at which Cyt *c* is conjugated to the ligand and the method used to conjugate Cyt *c* to the ligand. Previous work produced by Barfidokht et al., showed that increasing the distance between a redox molecule and an electron-rich node can reduce electron transfer abilities, as seen with ruthenium hexamine [18]. Although this system differs from the present case, the principle may still apply to Cyt *c* and the iron at the centre of the heme contained within the protein and is responsible for the electron transfer abilities. The method used to conjugate Cyt *c* to the ligand attached to the AuNPs could also influence the redox ability of the protein by changing its structure or orientation. Previous work by us showed that modifying the ligand's termination functional group influenced the orientation of Cyt *c* [19]. The terminated functional groups of carboxyl, hydroxyl and amino have negative, neutral, and positive zeta potentials (ζ). The different charged functional groups would then be attracted to differently charged amino acid residues in Cyt *c*, modulating its orientation. The AuNPs with carboxyl terminated ligands were shown to have had a more significant electrostatic interaction with lysine (Lys). In contrast, the hydroxyl and amino groups were shown to have an electrostatic interaction with glutamic acid (Glu). The cysteine (Cys) residues had been previously reported to

be located on the opposite side of the heme group of Cyt *c* to Glu and leucine (Leu), and by using time-of-flight secondary mass spectrometry (TOF-SIMS), the intensity values can then be used to help understand the orientation of Cyt *c* [19, 20]. The apoptotic potential of Cyt *c* when conjugated to AuNPs was found to be correlated with its orientation, with the heme group orientated towards the carboxyl group ligand termination demonstrating the lowest ability to induce apoptosis in cancer cells [19]. The present work aims to examine the effect of electrostatic and covalent conjugation on the redox ability of Cyt *c*. The hypothesis that stronger covalent conjugation may influence the secondary and tertiary structures of Cyt *c*, potentially affecting its redox ability is the driving force. In addition, we examined how the inclusion of zinc(II) 5-(4-aminophenyl)-10,15,20-tris-(4-sulfonatophenyl)porphyrin (Zn Porph) in the conjugation with AuNPs impacts the redox ability of Cyt *c* [14] [15]. (schematic representation of the functionalised AuNPs shown in Figure 1A and 3D structural representation of Cyt *c* in different redox states is shown in Figure 1B) [14] [15]. Recent studies conducted by the Rawson team highlight the promising potential of this AuNP system, It not only offers prospects for wirelessly activated cancer therapy but also stands as a frontrunner in the realm of quantum-based medical diagnostics and treatments [21].

Furthermore, this study aimed to identify the physical and electrochemical effects that immobilising Cyt *c* to AuNPs has upon the redox ability of the protein by varying the conjugation strategies, self-assembled monolayer (SAM) ligands, AuNP size, and presence of other adsorbate molecules. Using circular dichroism (CD) spectroscopy, we observed changes in the secondary and tertiary structures of Cyt c after its conjugation to AuNPs [16,17]. This technique can help monitor any modifications in a protein's structure, such as folding or unfolding [18]. Also, time-of-flight secondary ion mass spectrometry (ToF-SIMS) was used to discern the molecular composition of the surface, thereby helping us understand the orientation of Cyt c [19]. By

5

employing these techniques in conjunction, we linked any observed changes in structural orientation to potential shifts in the redox capacity of Cyt *c* [20]. The evaluation of electrochemical properties was conducted using both cyclic voltammetry (CV) and differential pulse voltammetry (DPV). The heterogeneous rate constant (k^0) for Cyt *c* or Zn Porph was calculated using Cyt *c*.
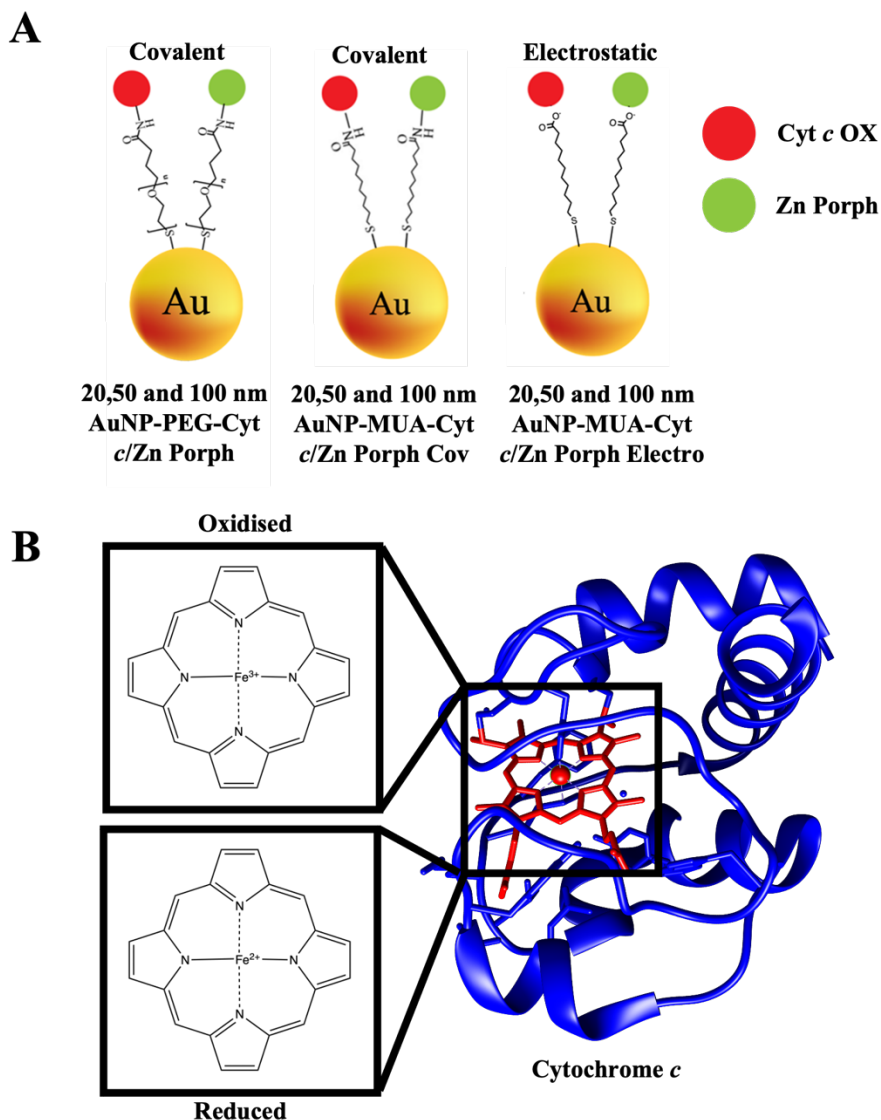
Figure 1: Schematic representation of AuNPs multifunctionalised with Cyt *c* and Zn Porph 20, 50 and 100 nm AuNP-PEG-Cyt *c*/Zn Porph, 20, 50 and 100 nm AuNP-MUA-Cyt *c*/Zn Porph Cov and 20, 50 and 100 nm AuNP-MUA-Cyt *c*/Zn Porph Electro (A). 3D structure crystal of Cyt *C* made from PDB (1 HRC) using Chimera (version 1.16) with blue representing amino acid residues and red representing the Heme ring. The heme group in different oxidative states is also shown (C).

2. Materials and Methods

Materials

Equine heart cytochrome c (Cyt c) ($\geq$ 95%), 1-Ethyl-3-(3-dimethylaminopropyl)carbodiimide hydrochloride (EDC), gold(III) chloride trihydrate ($HAuCl_4 \cdot 3H_2O$) (99.99%), thiol-PEG-carboxyl (HS-PEG-COOH) (2000 Da), 2-(N-morpholino)ethanesulfonic acid, 4-morpholine ethanesulfonic acid monohydrate (MES monohydrate) (99.0%), 11-mercaptoundecanoic acid (MUA), N-hydroxysuccinimide (NHS) (98%), sodium citrate tribasic dihydrate (99%) were purchased from Sigma Aldrich. 5-(4-Aminophenyl)-10,15,20-tris-(4-sulfonatophenyl)porphyrin (Porph) and zinc(II) 5-(4-aminophenyl)-10,15,20-tris-(4-sulfonatophenyl)porphyrin (Zn Porph) were purchased from Porphychem, France. Milli-Q® water at a resistivity of 18.2 MΩ provided by the Milli-Q® direct water purification system was used for all experiments.

4.1. Synthesis of 20 nm citrate capped AuNPs (cit-AuNPs)

An aqueous solution (1 mL) of $HAuCl_4 \cdot 3H_2O$ (39.38 mg, 0.1 mol) was added to of Milli-Q® water (89 mL) and was brought to a boil under constant stirring. Aqueous sodium citrate solution (38.8 mM, 10 mL) was rapidly added to the boiling solution, causing a colour change from yellow to burgundy. The solution was boiled for 10 minutes before allowing it to cool down at room temperature under stirring. The solution was then filtered using a 0.22 μm nylon filter to remove large aggregates and stored at 4 °C until further use.

4.2. Synthesis of 50 nm citrate capped AuNPs (cit-AuNPs)

A total of 100 µL of HAuCl$_4$·3H$_2$O (1% W/V) was added to a scintillation vial containing 9.488 mL of Milli-Q® water, before the addition of 20 nm AuNPs (290 µL) which was then set to stir at room temperature for 10 minutes. 22 µL of Sodium citrate tribasic dihydrate (1% W/V) was then added to the stirring solution and immediately followed by the addition of 100 µL of hydroquinone (30 mM). The solution rapidly changed colour and was mixed for a further 10 minutes. The obtained coloured solution was filtered using 0.22 µm filter and stored at 4 °C until further use.

4.3. Synthesis of 100 nm citrate capped AuNPs (cit-AuNPs)

A total of 100 µL of HAuCl$_4$·3H$_2$O (1% W/V) was added to a scintillation vial containing 9.748 mL of Milli-Q® water before the addition of 20 nm AuNPs (30 µL), which was then set to stir at room temperature for 10 minutes. 22 µL of Sodium citrate tribasic dihydrate (1% W/V) was then added to the stirring solution and immediately followed by the addition of 100 µL of hydroquinone (30 mM). The solution rapidly changed colour and was mixed for a further 10 minutes. The obtained coloured solution was filtered using a 0.22 µm filter and stored at 4 °C until further use.

4.4. Functionalisation of 20, 50 and 100 nm cit-AuNPs with PEG

A 1 mL solution of aqueous thiol-PEG-carboxyl (2000 Da, 1 mM) was added to 20 mL of 20 nm or 50 nm cit-AuNPs under stirring and left overnight. The following day the solution was washed twice using centrifugation at 13,400 rpm for 30 minutes to form a pellet of AuNP functionalised with PEG-COOH (AuNP-PEG). The pellet was then resuspended in ultrapure water and stored at

4 °C until further use.

4.5. Functionalisation of 20, 50 and 100 nm cit-AuNPs with PEG, Cyt c and Zn Porph

For covalent conjugation of Cyt *c* and Zn Porph on to 20, 50 and 100 nm AuNPs, a fresh EDC/NHS mix solution was made by adding EDC (19.17 mg, 100 µmol) and NHS (23 mg, 200 µmol) in 1 mL of MES buffer (10 mM, pH 5). A total of 100µL of EDC/NHS mix was added to the 1 mL aqueous solution of thiol-PEG-carboxyl (2000 Da, 1 mM) and was left stirring for 1 hour. To this solution, aqueous Cyt *c* (1 mL, 200 µM) and aqueous Zn Porph (1 mL, 200 µM) were added under constant stirring, the solution was then left stirring for 24 hours. For the synthesis of AuNP-PEG-Cyt *c,* only Cyt *c* (1 mL, 200 µM) was added, and in AuNP-PEG-Zn Porph, only Zn Porph (1 mL, 200 µM) was added to the EDC/NHS activated thiol-PEG-carboxyl. After the solution was stirred for 24 hours, 20 mL of 20, 50 or 100 nm cit-AuNPs were added and mixed for a further 24 hours. The solution was centrifuged at 13,400 rpm for 3 cycles using Milli-Q® water to remove any unbound Cyt *c* and Zn Porph. The obtained pellet was resuspended in 1 mL of Milli-Q® water to yield AuNP-PEG-Cyt *c*/Zn Porph.

4.6. Deconvolution modelling of Cyt c and Zn Porph conjugated to AuNPs

Deconvolution of the UV-visible absorption spectrum to confirm the conjugation of Cyt *c* and Zn Porph was performed using CASA-XPS. The absorption spectra of the chosen samples were imported into CASA-XPS as text files. The graph was then plotted, and the x-axis was changed to start with the smallest number near the origin. The region of interest was then selected using the

regions tool, and the background setting was changed to 'linear' as this closely represents how the spectra would look without the conjugated molecules. The convoluted peaks in the spectra were then found using the components tab, by adding the components that were thought to be in the region. The components were fitted to the spectra using the Levenberg-Marquardt algorithm LN (LN-MIE-Gans) fitting. The resulting spectra data was copied to Microsoft Excel before being added to GraphPad Prism 9 for analysis.

4.7. Functionalisation of 20, 50 and 100 nm cit-AuNPs with MUA

A 1 mL solution of MUA (1 mM) in 90:10 Milli-Q® water: ethanol was added to 20 mL of 20 nm or 50 nm cit-AuNPs under stirring and left overnight. The following day the solution was washed twice using centrifugation at 13,400 rpm for 30 minutes to form a pellet of AuNP functionalised with MUA (AuNP-MUA). The pellet was then resuspended in ultrapure water and stored at 4 °C until further use.

4.8. Functionalisation of 20, 50 and 100 nm cit-AuNPs with MUA, Cyt c and Zn Porph Covalently

For covalent conjugation of Cyt *c* and Zn Porph onto 20, 50 and 100 nm AuNPs, a fresh EDC/NHS mix solution was made by adding EDC (19.17 mg, 100 µmol) and NHS (23 mg, 200 µmol) in 1 mL of MES buffer (10 mM, pH 5). A total of 100µL of EDC/NHS mix was added to the 1 mL of MUA (1 mM) in a 90:10 Milli-Q® water: ethanol solution and was left stirring for 1 hour. To this solution, aqueous Cyt *c* (1 mL, 200 µM) and aqueous Zn Porph (1 mL, 200 µM) were added under constant stirring and left stirring for 24 hours. Then, 20 mL of 20, 50 or 100 nm cit-AuNPs were

11

added and mixed for a further 24 hours. The solution was centrifuged at 13,400 rpm for three cycles using Milli-Q® water to remove any unbound Cyt *c* and Zn Porph. The obtained pellet was resuspended in 1 mL of Milli-Q® water to yield a dispersed sample of AuNP-MUA-Cyt *c*/Zn Porph Cov.

4.9. Functionalisation of 20, 50 and 100 nm cit-AuNPs with MUA, Cyt c and Zn Porph Electrostatically

For electrostatic conjugation of Cyt *c* and Zn Porph on to 20, 50 and 100 nm AuNPs, aqueous Cyt *c* (1 mL, 200 μM) and aqueous Zn Porph (1 mL, 200 μM) were added to the 1 mL of MUA (1 mM) in a 90:10 Milli-Q® water:ethanol solution and left stirring for 24 hours. Then, 20 mL of 20, 50 or 100 nm cit-AuNPs were added and mixed for a further 24 hours. The solution was then centrifugation at 13,400 rpm for three cycles using Milli-Q® water to remove any unbound Cyt *c* and Zn Porph. The obtained pellet was resuspended in 1 mL of Milli-Q® water to yield a dispersed sample of AuNP-MUA-Cyt *c*/Zn Porph Electro.

4.10. ToF-SIMS

ToF-SIMS analysis was conducted in accordance with the work produced by Jain et al. [19]. Microscopy glass slides were cleaned with IPA and left to dry overnight before drop-casting the Cyt c functionalised AuNPs onto them. ToF-SIMS analysis was performed on each AuNP sample using a TOF SIMS IV system from ION-TOF GmbH (Münster, Germany), acquiring spectra for positively charged secondary ions. A 25 keV Bi3+ primary ion beam was used in the high current bunched mode to deliver 0.3 pA, and raster scanning was performed 30 times over a 100 x 100

12

µm² area, with a total dose kept below the static limit of 10^{12} ions/cm². To prevent charge build-up, a low-energy (20 eV) electron flood gun was used. The ToF analyser was set to a 200 µs cycle time, providing a mass range of 0-3492 mass units. Six spectra were collected from different regions of each sample, and control spectra of only cit-AuNPs were also obtained.

4.11. Circular Dichroism

CD spectra were recorded in the far and near UV as well as the Soret region at 20 °C on a Chirascan CD spectrophotometer (Applied Photophysics) equipped with a temperature control unit TC125 (Quantum Northwest). All the AuNP samples functionalised with Cyt *c* and Cyt *c Ox and Red free in solution* were dispersed in 10 mM PBS at pH 7.4. Three spectra were taken for each sample and averaged. A quartz cuvette with an optical path length of 1 mm was employed for all CD measurements.

4.12. Cyclic Voltammetry:

Cyclic voltammetry was conducted on a Metrohm Autolab M204 potentiostat in a three Electrode setup which was placed within a Faraday cage. The counter electrode consisted of a platinum wire, the reference electrode was Ag/AgCl saturated KCl, and the working electrode was indium tin oxide (ITO). ITO-coated glass was cut to approximately 10mm x 20mm, washed with acetone, isopropan-2-ol and water and dried with Nitrogen gas. The ITO was then assembled in an electric chemical cell with an exposed working area of 38.48 mm^2 defined by a silicone "O" ring. A new ITO working electrode was used for every sample. The Cyt *c* free in solution and AuNPs with conjugated Cyt *c* were dispersed in PBS at varying concentrations determined by UV-Vis

spectroscopy. CVs were conducted at a potential range of -0.2 V to 0.4 V with a start potential of -0.2 V and switching of 0.4 V and end of -0.2 V and -0.2 V to 1.2 V with a start potential of -0.2 V and switching of 1.2 V and end of -0.2 V using scan rates varying between 50 mV.s^{-1} to 2 V.s^{-1}.

4.13. Cyclic Voltammetry Analysis

The peak current and potential position for both redox peaks were calculated in Origin Pro. Firstly, the data was split into two sections; the oxidation peak data, which ranged from -0.2 to 0.4 V, and the reduction peak data from 0.4 to -0.2 V (the second part of the potential cycle). Each section of the cyclic voltammogram was then plotted and the background was subtracted. To background subtract, a 4th order polynomial fit was selected, and nodes were placed along the cyclic voltammogram to act as anchors. The region of interest for Cyt *c*, between -0.1 V and 0.2 V, was left clear of nodes in both the oxidation and reduction data sets, allowing a background to be created in this region. The interpolation method was changed from line to Spline and the background was then subtracted. The resulting data was plotted in GraphPad Prism 9, and the area under the graph function was used to obtain the peak height and position. This was repeated for the oxidation and reduction peaks for the scan rate of each sample.

4.14. Differential Pulse Voltammetry

Differential pulse voltammetry was conducted in accordance with section 4.12, with the exception of running the potential from -0.2 V to 0.4 V or -0.2 to 1.2 V for the oxidation peaks. The potentials were then reversed for the reduction peaks. Scan rates varied from 50 mV.s^{-1} to 10 mV.s^{-1}. A

voltage amplitude of 25 mV was used for all samples.

4.15. Differential Pulse Voltammetry Analysis:

The peak current and potential position for both redox peaks was calculated in Origin Pro. The data sets for the redox peaks were stored as different files as DPV increases or decreases potential in a linear sweep, therefore the data does not have to be split as in section 4.13. The oxidation data ranged from -0.2 V to 0.4 V for Cyt *c* free in solution or bound to AuNPs, and from -0.2 V to 1.2 V when the system contained both Cyt *c* and porphyrins free in solution or bound to AuNPs. For the reduction data, the inverse potentials were applied from 0.4 V to -0.2 V for Cyt *c* free in solution or bound to AuNPs, and from 1.2 V to -0.2 V for the Cyt *c* and porphyrins free in solution. Each section of the cyclic voltammogram was then plotted, and the background was subtracted. To background subtract, a 4th order polynomial fit was selected, and nodes were placed along the cyclic voltammogram at points acting as anchors. The region of interest for Cyt *c* between -0.1 V and 0.2 V was left clear of nodes, allowing a background to be created in this region. The region of interest for the porphyrins ranged between 0.3 V to 0.6 V for the first redox peak, and 0.7 V to 1 V for the second peak; both regions were left clear of nodes allowing a background to be created in both. The interpolation method was changed from line to Spline and the background was subtracted. The resulting data were plotted as a new graph in Origin Pro and using the quick peaks tool the region of interest mentioned previously was selected. The baseline mode was set to 2nd derivative with the range of curve within ROI selected, and the smoothing method used for the baseline was adjacent averaging with a maximum of 8 anchor points and the connect method set as the line. The peak finding method was set to a local maximum determined by 15 local points, and peak filtering was turned on to a threshold height of 20%. Once the peaks were identified by

the software, their heights and position were output to a table.

3. Results

3.1. *Investigation on the structural change of Cyt c after conjugation to AuNPs of different sizes using different ligands and conjugation methods.*

AuNP synthesis, characterisation and functionalisation have been previously reported and schematic representation of the functionalised AuNPs, Cyt *c* and Zn Porph are represented in that work [22]. Deatiled physical charteristaion of the funtionalised partciles can be seen in Figure s1. To investigate the structure of native Cyt *c* in solution we performed CD analysis at two different concentrations, 20 μM and 1 μM, to determine whether the intensity of maxima and minima peaks changed as the signal-to-noise ratio changed (lower Cyt *c* concentration should have a larger signal-to-noise ratio) (Figure 2A-F). The higher concentration of Cyt *c* was used to obtain an accurate CD spectrum, while the lower concentration was employed to represent the amount of Cyt *c* that is usually conjugated to AuNPs. In the far-UV CD spectra (in the range of 180-260 nm), the double minima in molecular ellipticity located at 208 and 222 nm and the positive band at ~190 nm can be identified for Cyt *c* Ox and Red in both 20 μM (Figure 2A) and 1 μM (Figure 2D). The double minima and positive band indicate the alpha-helical content, which can be associated with the catalytic ability of the protein [23]. The double minima are more defined for Cyt *c* Red than Cyt *c* Ox in both Figure 2A and Figure 2D, insinuating a greater alpha helical content. The near-UV CD spectra in the range of 260-360 nm showed a double minimum at 282 nm 288 nm for both Cyt *c* Ox and Red at 20 μM (Figure 2 B), which can be associated with Tryptophan residues indicative of the tertiary structure [24]. Only the minimum at 288 nm is visible in Cyt *c* Ox and

Red at 1 μM, with the 282 nm band appearing to blue shift to ~275 nm (Figure 2E), as the signal-to-noise ratio must be large to detect this minimum at 282 nm. The CD spectra were also obtained in the Soret region (360-450 nm), enabling further understanding of the tertiary structure of Cyt *c,* as the Soret region can be attributed to the heme ring of Cyt *c* (Figure 2C and F). The 20 μM Cyt *c* Ox and Red showed maxima at 405 and 408 nm, respectively, with minima both at 416 nm. 20 μM Cyt *c* Red also displayed an additional maximum at 431 nm (Figure 2C). For 1 μM Cyt *c* Ox and Red, the maxima and minima were blue shifted to 403 and 412 nm, respectively, with 1 μM Cyt *c* Red displaying the same maxima as 20 μM Cyt *c* Red at 431 nm. This data, therefore, shows that lower Cyt *c* concentrations, comparable to those observed in AuNP samples conjugated with Cyt *c,* produce high signal-to-noise background resulting in spectra of near-UV CD and Soret region CD that are more difficult to interpret. CD was conducted for Cyt *c* conjugated to AuNPs using HS-PEG-COOH covalently (with EDC/NHS), MUA covalently (with EDC/NHS), and MUA electrostatically to investigate the conjugation's effect on the structure of the protein.
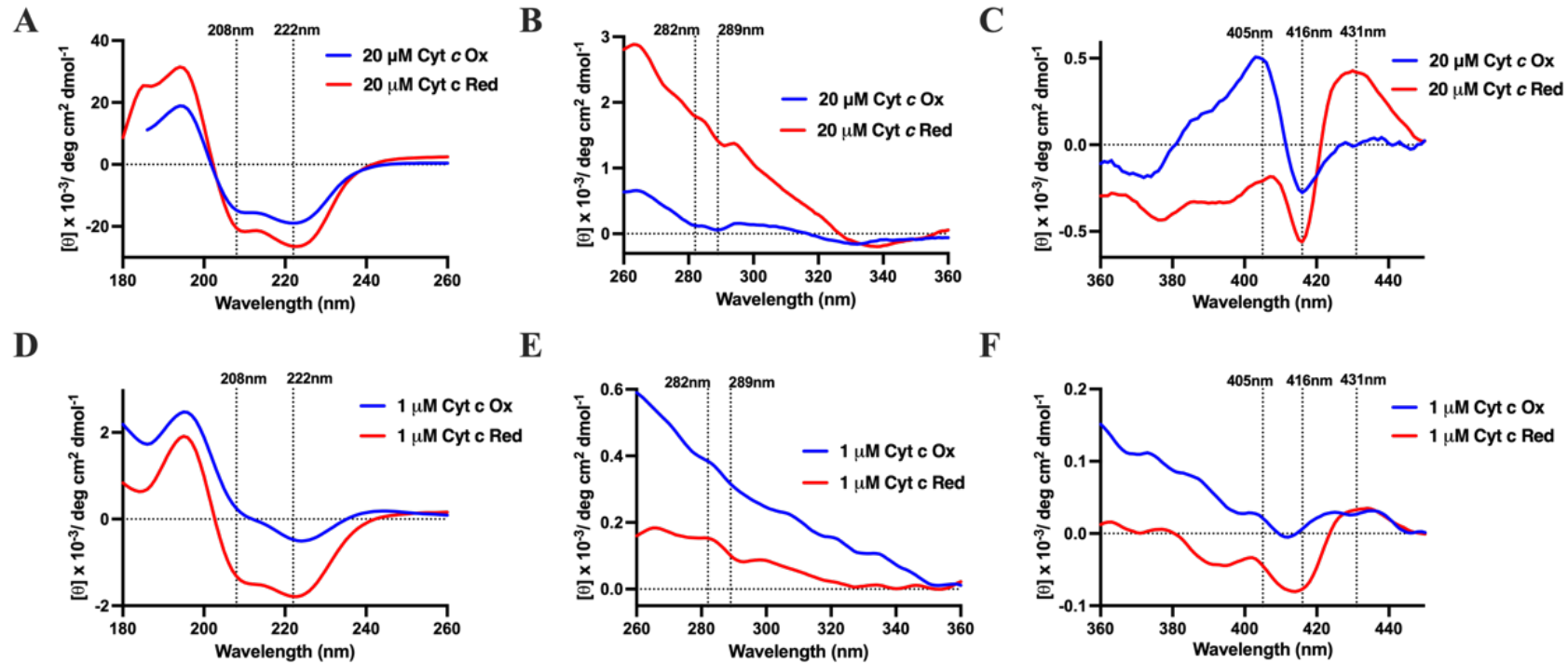
Figure 2. Comparison between the CD spectra of 20 µM Cyt c. The CD spectra of 20 µM Cyt c Ox and Red in the far-UV region (A), near-UV region (B) and Soret region (C). The CD spectra of 1 µM Cyt c Ox and Red in the Far-UV region (D), near-UV region (E) and Soret region (F)

3.2. Investigation on the structural change of Cyt c after conjugation to AuNPs of different sizes using different ligands and conjugation methods.

It was important to establish the secondary structure of the Cyt *c* when bound to gold nanoparticles using covalent tethering to AuNPs via functionalisation with MUA and HS-PEG-COOH conjugation through carbodiimide coupling chemistry and physiosorbed to the same surface. Cyt *c* covalently bound to AuNPs using HS-PEG-COOH as ligand and conjugated with the use of EDC/NHS, the far-UV region for all of the samples (Figure 3A) demonstrated clear minima at 208 and 222 nm, the same positions seen with Cyt *c* free in solution (Figure 2A and D), suggesting no change in the secondary structure of Cyt *c*. The CD spectra for the 20 nm AuNPs are more defined; this feature is most compatible with Cyt *c* Red, despite Cyt *c* Ox being used in this functionalisation method. (Figure 3A). Cyt *c* was coupled to the nanoparticles using MUA as a ligand and conjugating with EDC/NHS coupling chemistry, showed less well-defined CD spectra when compared to Cyt *c* free in solution (Figure 2A and D), although the position of one minimum at 208 nm was maintained (Figure 3D). Despite this feature, the minima at 222 nm in the free protein were red-shifted to 227 nm, suggesting a change in alpha-helical content and, therefore, an alteration in the secondary structure of the 20, 50 and 100 nm AuNPs. Cyt *c* was physiosorbed to AuNPs functionalised with MUA via electrostatic interactions presented minima at 208 nm but showed the 222 nm minima to be red-shifted to 225 nm for the 20 nm AuNPs, and to 227 nm for 50 and 100 nm AuNPs, once again suggesting changes in alpha-helical content and subsequently in the secondary structure (Figure 3G). The definition of the CD far-UV spectra becomes less as the AuNP size deceased for Cyt *c* conjugated to MUA electrostatically, likely the result of a lower overall

content of Cyt *c* in the samples with larger AuNPs. The CD spectra in the near-UV region showed double minima at 282 nm and 289 nm for all Cyt *c* conjugated to AuNPs using HS-PEG-COOH (Figure 3B) and MUA covalently (Figure 3E), indicating tertiary structure (signified by Tryptophan residues) remained unchanged (Figure 2B and E). The 20 and 100 nm AuNP-MUA-Cyt *c* Electro samples also showed these double minima at 282 nm and 289 nm, suggesting they too have an unchanged tertiary structure. In contrast, these minima are not visible for 50 nm AuNP-MUA-Cyt *c* Electro, indicating a change in the tertiary structure of this sample. The CD spectra in the Soret region for Cyt *c* conjugated to AuNPs (Figure 3C, F and I for Cyt *c* conjugated to AuNPs using HS-PEG-COOH covalently, MUA covalently, and MUA electrostatically, respectively) differed from that observed of the Cyt *c* free in solution (Figure 2C and F). The positive maxima for Cyt *c* conjugated to AuNPs with HS-PEG-COOH were located at 403, 410 and 405 nm for 20, 50 and 100 nm AuNP samples respectively. The minima were not present in 50 nm AuNP samples but appeared at 420 nm for both the 20 and 100 nm samples (Figure 3C). These changes in the maxima and minima indicate a structural change around the heme moiety of Cyt *c*. The structural changes are similarly observed for both Cyt *c* conjugated to AuNPs using MUA covalently and electrostatically (Figure 3F and I), as the shape of the spectra and positions of maxima and minima all differ from Cyt *c* Ox or Red free in solution.
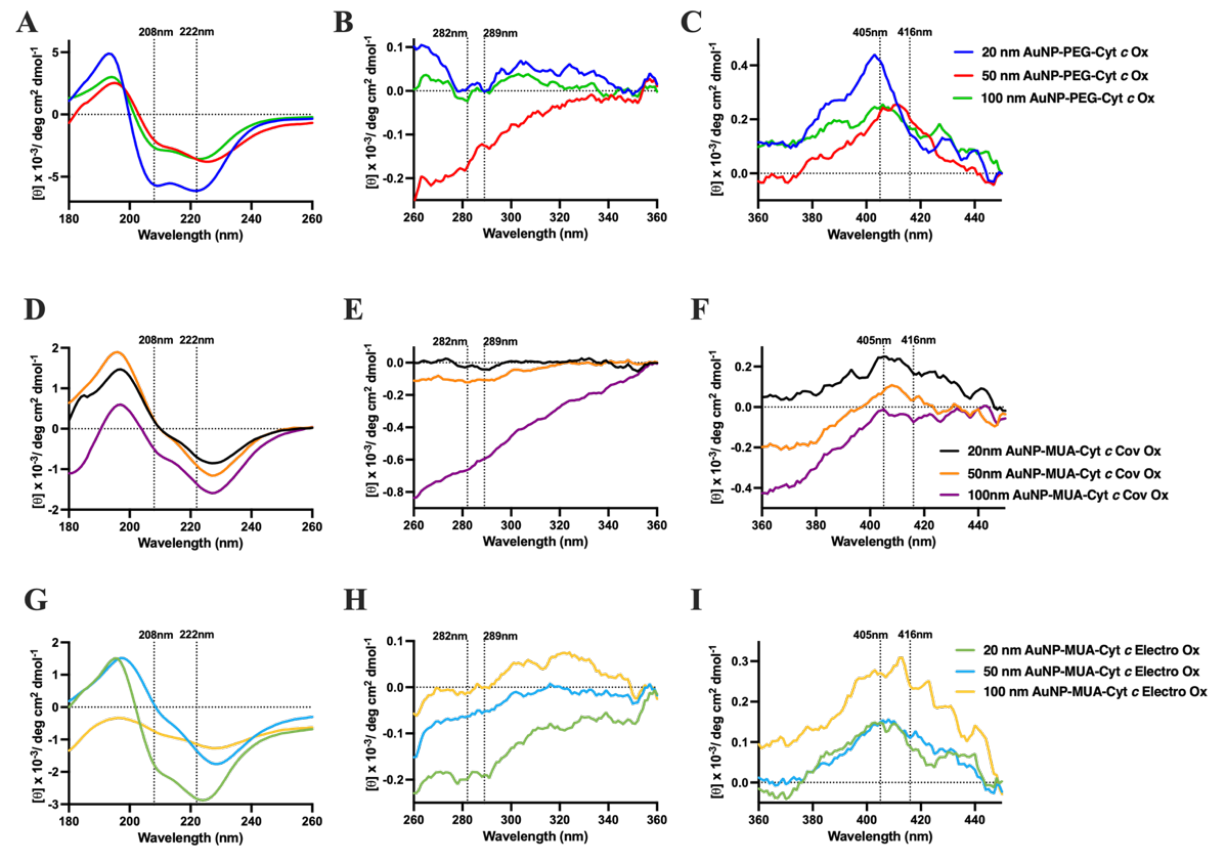
Figure 3. Comparison between the CD spectra of Cyt c conjugated to AuNPs using HS-PEG-COOH covalently (with EDC/NHS), MUA covalently (with EDC/NHS) and MUA electrostatically. 20, 50 and 100 AuNP-PEG-Cyt c in the Far-UV region (A), near-UV region (B) and Soret region (C). 20, 50 and 100 AuNP-MUA-Cyt c Cov in the far-UV region (D), near-UV region (E) and Soret region (F). 20, 50 and 100 AuNP-MUA-Cyt *c* Electro in the Far-UV region (G), near-UV region (H) and Soret region (I).

The CD spectra indicate that Cyt *c* undergoes structural changes when conjugated to AuNPs using different ligands and methods of conjugation. It was observed that Cyt *c* conjugated to AuNPs using thiol-PEG-carboxyl experienced minimal changes, as evidenced by alterations in only the CD spectra in the Soret region (indicating modifications in the heme group's structure). However, when Cyt *c* was conjugated to AuNPs using MUA through covalent and electrostatic interactions, the secondary and tertiary structures of Cyt *c* were altered. No specific correlation could be identified to determine the effect of the conjugation method, as Cyt *c* showed similar secondary and tertiary distortion when conjugated to AuNPs both covalently and electrostatically. The significant difference between Cyt *c* conjugated to AuNPs with HS-PEG-COOH and MUA is the length of the ligand. The length of 2 kDa PEG was predicted to be ~7.9 nm, whereas MUA had a predicted length of ~1.4 nm (determined via ChemDraw3D). The increased structural distortion in the Cyt *c* bound to AuNPs with MUA covalently and electrostatically may be the result of the AuNPs themselves, because of their proximity to the protein. AuNPs have strong absorption and light scattering abilities in the visible and near-UV region, which could account for the difficulty foreseen in determining maxima and minima and be the result of spectral shape changes.

3.3. ToF-SIMS

We then used ToF-SIMS to investigate whether the orientation of Cyt *c* conjugated to AuNPs varied with different AuNP sizes and ligandation type. Earlier studies found that cysteine residues (Cys) were situated close to the heme moiety of Cyt *c*, while glutamic acid (Glu) and leucine residues (Leu) were located on the opposite side of the heme moiety [20]. The study used ToF-SIMS to compare the secondary ion intensity related to cysteine residues to that of glutamic acid and leucine. The researchers were then able to determine the orientation of Cyt *c* by calculating the ratio

22

R=ICys/(ILeu+IGlu) [20]. By virtue of this previous work, we proposed that Cyt *c* within AuNP-COOH-Cyt *c* would have an orientation in which the heme ring is positioned near the protein-ligand interface, with the positively charged residues lysine (Lys 79) electrostatically interacting with the carboxylic group [19]. This orientation would bring the Cys residues nearer to the carboxylic group, leading to reduced secondary ion intensity detected by ToF-SIMS. In both studies, it has been suggested that a change in R of ~50% or greater indicates a 180° rotation in orientation.

The ToF-SIMS peak intensity ratios R=ICys/(ILeu+IGlu) for Cyt *c* that is conjugated to 20, 50, and 100 nm diameter AuNPs using thiol-PEG-COOH covalently (with EDC/NHS), MUA covalently (with EDC/NHS), and MUA electrostatically is displayed in Figure 3A. The comparison is made against 100 nm AuNP-MUA-Cyt *c* Electro: the closest match to the work by Jain et al., 2021 which predicts the orientation of the heme of Cyt *c* to be towards the terminated carboxyl group [19]. The results of Jain's work show that 20 and 50 nm AuNP-MUA-Cyt *c* Electro and 20 nm AuNP-MUA-Cyt *c* Cov have an R difference of ~50% or greater, when compared to 100 nm AuNP-MUA-Cyt *c* Electro, indicating an orientational difference. The R-value suggests that Cys residues in the Cyt *c* of 20 and 50 nm AuNP-MUA-Cyt c Electro and 20 nm AuNP-MUA-Cyt *c* Cov have a higher intensity than Glu or Leu residues and thus must be orientated away from the AuNP. The longer ligand, thiol-PEG-carboxyl, did not show a change in R-value for Cyt *c* conjugated to any size AuNP, only the 20 and 50 nm AuNPs functionalised with MUA showed a change. These results indicate that the orientation of Cyt *c* is influenced by the AuNPs themselves and orientation change is more prevalent in the more weakly bound electrostatic samples. The samples with smaller AuNPs have more individual AuNPs contained in a given mass of Au, and so the positively charged Lys residues may be more influenced by the electron rich AuNPs in the solution. The Lys residues are mostly

23

located near the Cys residues, exposing the heme ring more and producing a higher Cys residue intensity value. Glu is negatively charged and so may be repelled by the electron rich AuNPs and appears at a lower intensity as Glu and Leu (both located at the opposite side of the heme ring when compared to Cys) would be hidden more by the Cyt *c* structure for the samples with a more exposed heme ring.

The suggested orientations of Cyt *c* conjugated to AuNPs are displayed in Figure 4Figure 4B and C. The samples which did not show a large divergence in R-value when compared to 100 nm AuNP-MUA-Cyt *c* Electro are presented in Figure 4Figure 4B with the ligand termination conjugated to Lys 79 following Jain et al., 2021 [19]. The Lys residues are a likely point for conjugation as they are positively charged, so would naturally have electrostatic interaction with the carboxyl group, while also containing amino groups which are required for covalent conjugation using EDC/NHS [25]. Lys 25 and 27 are also highlighted as they too are potential conjugation sites and may be the result of variation in the amino acid intensity values. The predicted orientation of 20 and 50 nm AuNP-MUA-Cyt *c* Electro and 20 nm AuNP-MUA-Cyt *c* Cov is represented in the schematic from Figure 4Figure 4C.C. Conjugation to Lys 88 would cause the heme group to be more exposed, resulting in increased Cys residue intensity and a lower Glu and Leu intensity.
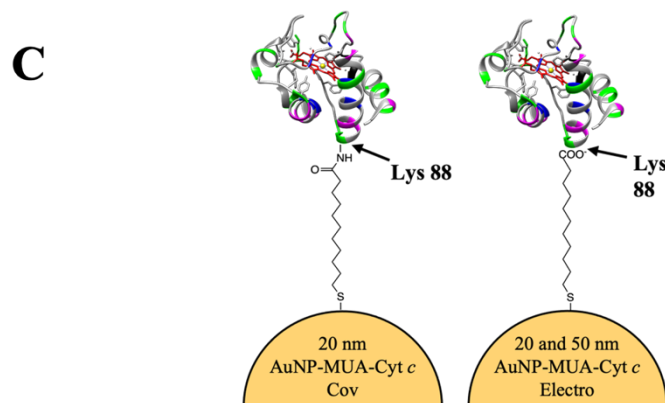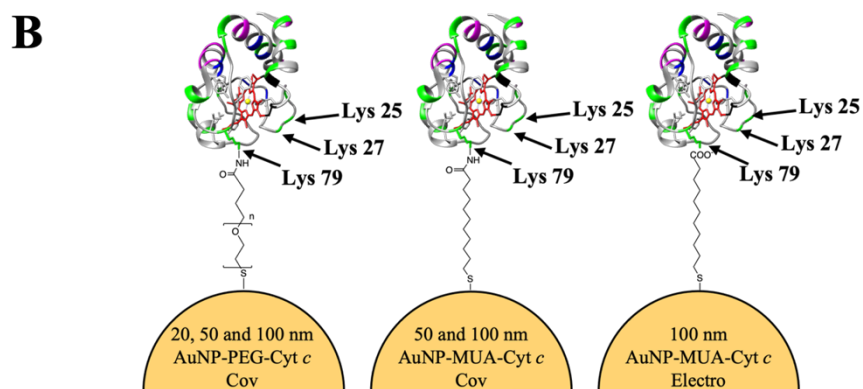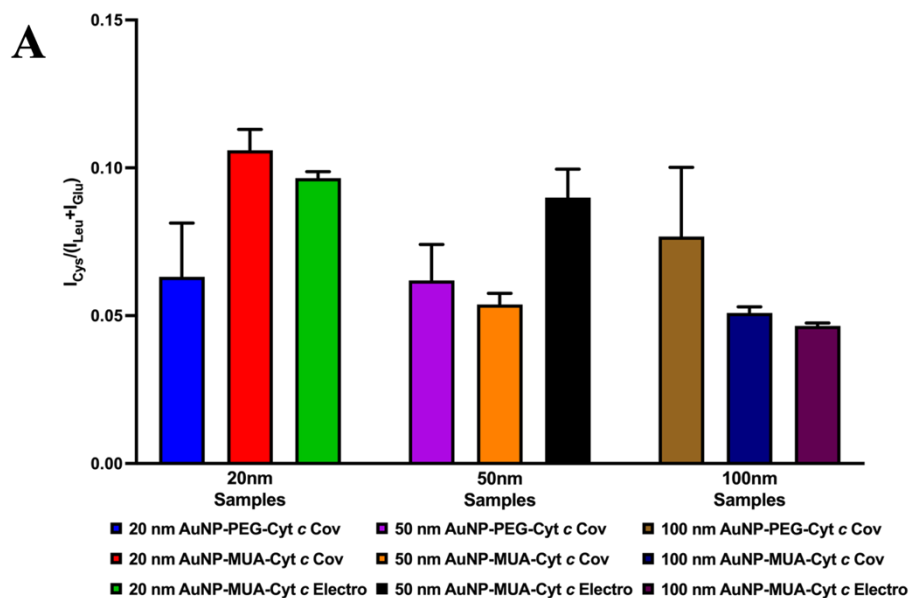
Figure 4. ToF-SIMS peak intensity ratio for cysteine/glutamic acid + leucine for Cyt *c* free in solution

and bound to 20 nm AuNPs using different ligands and conjugation strategies (A).

The orientation of Cyt *c* when attached to AuNPs using PEG and MUA ligands covalently or electrostatically was proposed using ToF-SIMS amino acid intensity ratio and literature (Jain et al., 2021). Both covalent and electrostatic conjugation methods identified the binding of AuNPs to the Lys 79 residue of Cyt *c*, with Lys 27 and Lys 25 potential alternatives (B). The proposed orientation for Cyt *c* bound to AuNPs at the Lys 88 residue was determined when the R value differed by ~50% or greater compared to 100 nm AuNP-MUA-Cyt *c* Electro (C). A 3D model of Cyt *c* was created using the crystal structure of horse heart Cyt *c* from the PDB (1HRC) in Chimera (version 1.15) to label the heme ring and amino acid residues. In the structure of Cyt *c*, the heme/porphyrin ring was red, the Iron (Fe) at the centre of the heme\porphyrin ring was yellow, Cys was black, Glu was magenta, Leu was blue, and Lys was green.

3.4. Cyclic Voltammetry

Cyclic voltammetry (CV) was conducted on Cyt *c* free in solution (2 μM) and Cyt *c* conjugated to AuNPs to establish whether the redox ability of Cyt *c* is retained after conjugation. The heme group in Cyt *c*, containing iron at its centre, is responsible for the observed redox couple at approximately 0.09 V (oxidation peak) and 0.039 V (reduction peak), as shown in Figure 5 and supported by the literature [26]. The surface reactive groups of Cyt *c*, including carboxylic, amine, hydroxyl, and thiols, undergo protonation and deprotonation, but these events do not coincide with the redox peaks produced by the heme's Fe atom [27]. The heme group in Cyt *c* plays a crucial role in the protein's primary functions, such as within the electron transport chain, where it facilitates electron transfer from complex II to complex III. Cyt *c* is also involved in apoptosis, acting as the first reversible point to trigger the process via 'activation' of the Cyt *c,* resulting from a redox change caused by cellular damage or stress factors [1]. Any change in electrochemical activity may indicate a change in

26

function, hence it is essential to understand the cause of any changes. Figure 5A demonstrates that accurate determination of the redox peaks of Cyt *c* is not possible when it is conjugated to AuNPs, because clear signals are not apparent.

Cyclic voltammograms of Zn Porph were performed, showing typical CV features that are observed at a higher potential than those of Cyt *c* (Figure 5B); these are evident with *Epa* of 0.65 ± 0.01 and 0.95 ± 0.03 V, with only one reduction peak being identified at 0.60 V, represents irreversible electrochemistry. No observable redox electrochemistry associated with Zn Porph was apparent when the unit was coupled to the nanoparticles, due to masking by charging currents at the low concentrations necessary for the experiments. It was therefore concluded that the only way to accurately identify the redox peaks of Cyt *c* and Zn Porph when conjugated to AuNPs would be by reducing the charging current. We therefore postulated using differential pulse voltammetry (DPV) would overcome this problematic high charging current [28] allowing us to observe electrochemistry associated with the Zn Porph and Cyt *c* when bound to AuNPs.
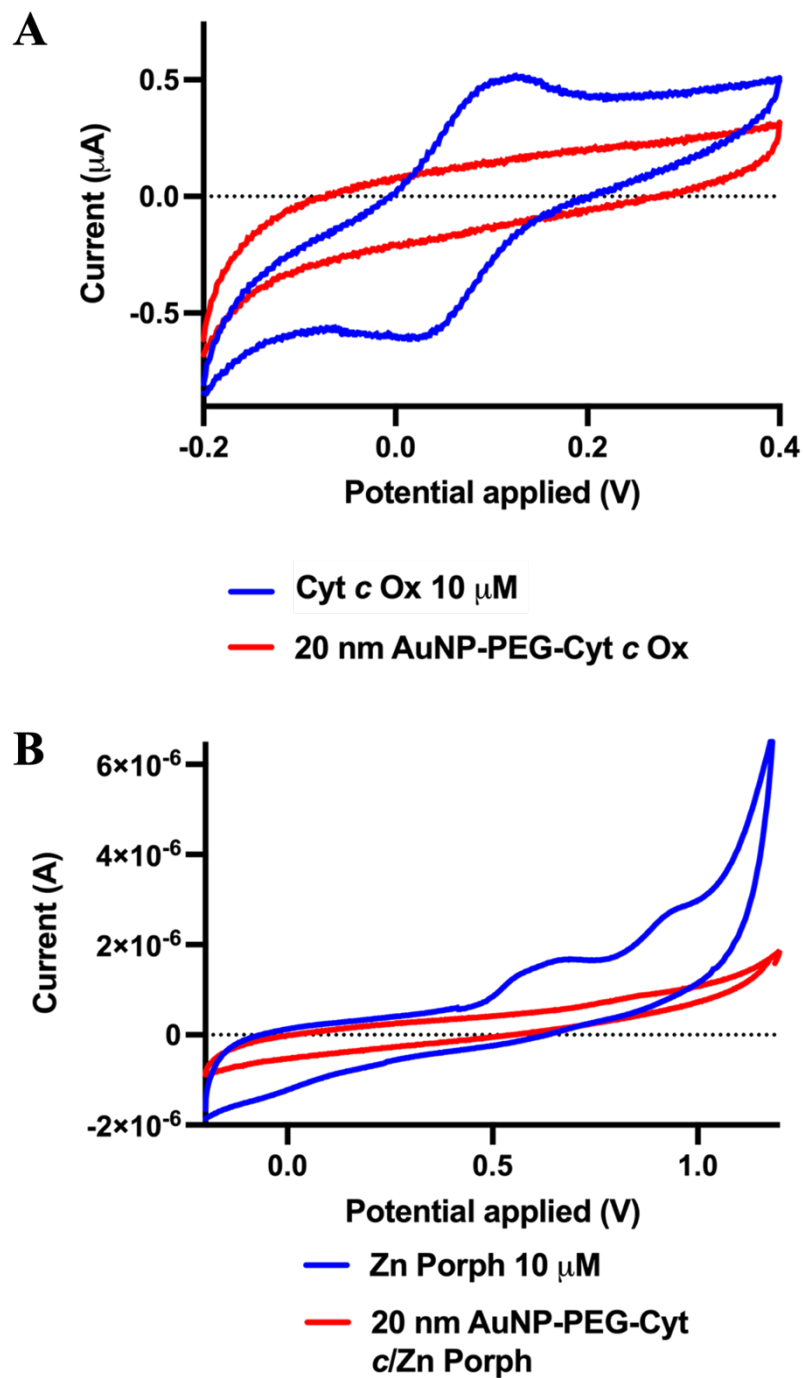
A

Cyt *c* Ox 10 μM

20 nm AuNP-PEG-Cyt *c* Ox

B

Zn Porph 10 μM

20 nm AuNP-PEG-Cyt *c*/Zn Porph

Figure 5. Cyclic voltammogram's at 0.1 V.s^{-1} of Cyt *c* Ox 10 μM free in solution and 20 nm AuNP-PEG-Cyt *c* Ox. Cyclic voltammograms' run from -0.2 to 0.4 V and PBS was used as the electrolyte (A). Cyclic voltammogram's at 0.1 V.s^{-1} of Zn Porph and 20 nm AuNP-PEG-Cyt *c*/Zn Porph. Cyclic

28

voltammograms' run from -0.2 to 1.2 V and PBS was used as the electrolyte (B).

3.5. Differential Pulse Voltammetry

We employed a novel approach to DPV, by setting out to identify the electron transfer rate between Cyt *c* and porphyrins, and the electrodes. A new analysis method was devised to precisely determine the height and position of the redox peaks for both Cyt *c* and Zn Porph. Previous work using 1.6 nm AuNPs coated with hexanethiolate ligands demonstrated a similar difficulty in identifying a defined peak in the CVs, however through DPV as many as 13 peaks could be resolved due to the suppression of working electrode background currents [29]. In the present[29]. In the present study, the new approach involved varying the scan rates of DPV on both the oxidation and reduction sweepssweeps, to obtain an electron transfer rate for each component when we have bi-functionalised AuNPs with Zn Porph and Cyt *c*.

3.6. Scan rate studies

Scan rates were varied from 50 to 10 mV/s, with the goal of calculating the electron transfer rate of Cyt *c* and Zn Porph conjugated to AuNPs. To calculate the electron transfer rate k^0, numerous equations were combined [30]. In the work produced by Hicks et al., 2017 the k^0 value was determined using k^0, numerous equations were combined [30]. In the work produced by Hicks et al., 2017 the k^0 value was determined using Equation 1 [31].

$$\psi = k^0 \left[\frac{\pi D n v F}{RT} \right]^{-0.5}$$

29

Equation 1.

Where ψ is a function of the peak separation, D is the diffusion coefficient, n is the number of electrons transferred in the redox reaction, v is the scan rate, F is the Faraday constant, R is the gas constant, and T is the temperature [31, 32]. Equation 1 was rearranged to find the heterogeneous rate constant as shown in Equation 2.

$$k^0 = \frac{\psi}{\left[\frac{\pi D n v F}{RT}\right]^{-0.5}}$$

Equation 2.

From Equation 2 there are still two unknown factors that needed to be determined to complete the equation, ψ and D. For calculating ψ, Equation 3 was used.

$$\psi = 2.18(\frac{\alpha}{\pi})^{0.5} exp\left[-\left(\frac{\alpha^2 F}{RT}\right)n\Delta E_p\right]$$

Equation 3.

Where a is the transfer rate coefficient, assumed to be 0.5 [31], and ΔE_p is the peak separation. Equation 2 and Equation 3 were then combined to give Equation 4

$$k^0 = \frac{2.18\left(\frac{\alpha}{\pi}\right)^{0.5} exp\left[-\left(\frac{\alpha^2 F}{RT}\right)n\Delta E_p\right]}{\left[\frac{\pi D n v F}{RT}\right]^{-0.5}}$$

30

Equation 4.

Where D is the diffusion coefficient, n is the number of electrons transferred in the redox reaction, F is the Faraday constant, R is the gas constant, T is the temperature [31, 32], a is the transfer rate coefficient assumed to be 0.5 following literature, and ΔE_p is the peak separation.

Only the value of D now remains unknown in calculating k^0; this can usually be determined using the Randles-Sevcik equation in cyclic voltammetry. However, a separate equation is used for DPV. The electrode surface area, A, has been calculated as 38.48 mm^2 in a previous study [19]. The concentration of the analyte, C, was determined through UV-Vis absorption spectroscopy, as outlined in our previous paper [22]; the number of electrons transferred in the redox event was assumed to be 1 for Cyt c [1, 33]; $\Delta\tau$ is the pulse duration, set at 50 milliseconds. σ is equal to $\exp\left(\frac{nF}{RT} * \frac{\Delta E}{2}\right)$; the temperature was recorded to be 22°C, room temperature. The equation was then rearranged to derive, the diffusion coefficient.

$$(\delta i)\max \ = \ nFAC\sqrt{\left(\frac{D}{(\pi * \Delta\tau)} * \frac{1-\sigma}{1+\sigma}\right)}$$

$$D = \frac{(\delta_i)^2 \max\ \pi\ \Delta\tau\ (1+\sigma)}{n^2 F^2 A^2 C^2\ (1-\sigma)}$$

$$D = \frac{(\delta_i)^2 \max\ \pi\ \Delta\tau\ (1+\exp(\frac{nF}{RT} * \frac{\Delta E}{2}))}{n^2 F^2 A^2 C^2\ (1-\exp(\frac{nF}{RT} * \frac{\Delta E}{2}))}$$

Equation 5.

31

A calculator for Equation 5 was produced using python and is included in the supporting information (Figure SI 2). Once the diffusion coefficient had been calculated, all the values could then be inputted into Equation 4 to give the k^0 value. The k^0 value was determined for Cyt c free in solution and bound to AuNPs using Equations 1-5.

For the measurement of magnitudes of peak current and peak potentials, a polynomial fit was applied to the background subtracted DPV of each sample (see SI for details). For the measurement of magnitudes of peak current and peak potentials, a polynomial fit was applied to the background subtracted DPV of each sample (see SI for details). 2003 discovered a correlation between the hydrogen bonding capability of the SAM and the k^0 value of Cyt c, suggesting that the k^0 value is dependent upon factors such as outer-sphere reorganisation energy, the double layer current (background current), and the electronic coupling between the different SAMs and Cyt c. Previous studies have shown that the k^0 values of Cyt c bound to gold electrodes via 11 different SAMs ranged from 10^{-4} to approximately 10^{-1} cm/s [34]. Liu et al., 2003 discovered a correlation between the hydrogen bonding capability of the SAM and the k^0 value of Cyt c, suggesting that the k^0 value is dependent upon factors such as outer-sphere reorganisation energy, the double layer current (background current), and the electronic coupling between the different SAMs and Cyt c. Given the similarities between the work of Liu et al. 2003 and this work, it was essential to determine the k^0 values of Cyt c bound to AuNPs of different sizes, with ligands of varying lengths, and various methods of conjugation [34]2003 and this work, it was essential to determine the k^0 values of Cyt c bound to AuNPs of different sizes, with ligands of varying lengths, and various methods of conjugation [34]. This analysis was crucial in determining whether any of these factors influenced the k^0 value. Moreover, comparing the k^0 value with biological data assisted in ascertaining whether

32

the k^0 value affects the apoptotic ability of Cyt *c*.

DPV tested the controls used in multifunctionalised AuNPs and determined whether the redox peaks of Cyt *c* and Zn Porph could be identified. As shown in Figure 6, the redox peaks for Zn Porph, Cyt *c* Ox, and Cyt c Red were all easily identifiable. However, only one peak was visible for Zn Porph, unlike in the results obtained in CV in which multiple peaks were shown. In the case of AuNPs and PBS, DPV did not show any redox peaks, except for a very small peak at ~1.0 V for 20 nm cit-AuNPs, which could potentially interfere with the DPV spectra of the 20 nm multifunctionalised Cyt *c* and Zn Porph, as a result no analysis was conducted in this region.
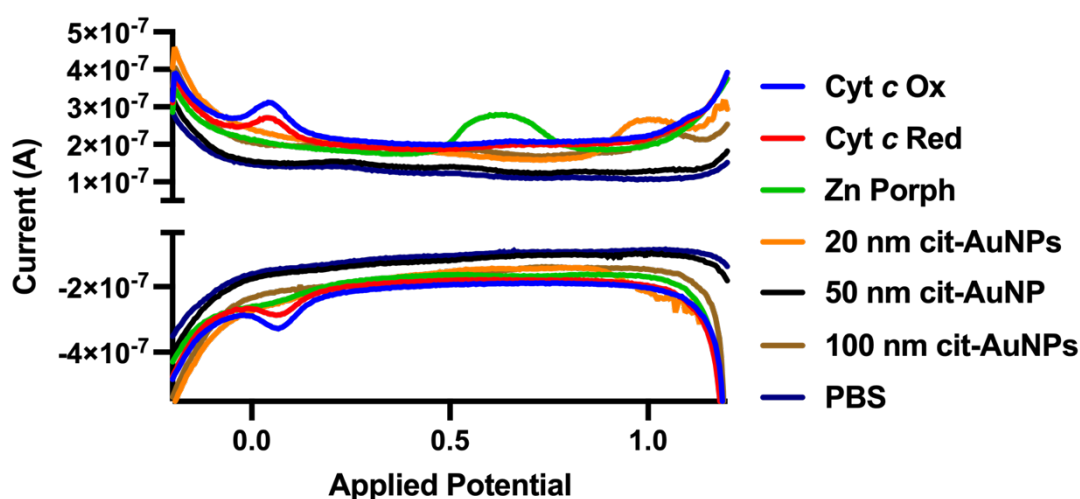

Figure 6. DPV of all control used in functionalised AuNPs measure between the potentials of -0.2 to 1.2 V using a scan rate of 50 mV/s.

The peak potentials of Cyt *c* identified using DPV differ from those determined by CV, likely due to variations in the techniques. DPV measures the current response to a series of voltage pulses, while

CV measures the current response to a linearly increasing or decreasing voltage sweep. The differences in the experimental conditions can cause variations in the observed peak potentials, as the behaviour of the electrode surface may differ between the two techniques [30]. For a reversible and fast, one-electron transfer, the expected peak-to-peak separation (ΔE_p) is known to be 57 mV at room temperature for CV measurements. Still, this value is rarely discussed in relation to DPV due to the single potential sweep that is used in DPV unlike the cyclic potential of CV's [33]. In the case of Cyt *c*, the ΔE_p values for the Ox and Red forms were calculated from The peak potentials of Cyt *c* identified using DPV differ from those determined by CV, likely due to variations in the techniques. DPV measures the current response to a series of voltage pulses, while CV measures the current response to a linearly increasing or decreasing voltage sweep. The differences in the experimental conditions can cause variations in the observed peak potentials, as the behaviour of the electrode surface may differ between the two techniques [30]. For a reversible and fast, one-electron transfer, the expected peak-to-peak separation (ΔE_p) is known to be 57 mV at room temperature for CV measurements. Still, this value is rarely discussed in relation to DPV due to the single potential sweep that is used in DPV unlike the cyclic potential of CV's [33]. In the case of Cyt *c*, the ΔE_p values for the Ox and Red forms were calculated from Figure 6 to be 19 and 27 mV, respectively, suggesting surface chemistry is confined in CV but that same understanding cannot be applied to DPV measurements [35]. These small ΔEp values suggest that a portion of the response is from surface confined Cyt *c*. In DPV Bard & Faulkner suggest that the surface concentration of analyte is regarded as the apparent bulk concentration of the pulse, suggesting that surface confined electrochemistry is not as important to identify in DPV as in CV to be 19 and 27 mV, respectively, suggesting surface chemistry is confined in CV but that same understanding cannot be applied to DPV measurements [35]. These small ΔEp values suggest that a portion of the response is from surface-confined Cyt *c*.

34

In DPV Bard & Faulkner suggest that the surface concentration of analyte is regarded as the apparent bulk concentration of the pulse, suggesting that surface confined electrochemistry is not as important to identify in DPV as in CV [36, 37]. The peak separation of Zn Porph was found to be 56 mV, indicating a fast, reversible two-electron transfer event in CV, but this may not be the case in DPV measurements.

Table 1. The DPV peak separation of Cyt *c* Ox, Cyt *c* Red and Zn Porph calculated from Figure 6. The oxidation potential

Control Sample	Oxidation Ep (V)	Reduction Ep (V)	ΔE_p (Peak Separation) (mV)
Cyt *c* Ox	0.048	0.067	19
Cyt *c* Red	0.050	0.077	27
Zn Porph	0.624	0.680	56

3.7. Differential Pulse Voltammetry on AuNPs functionalised with Cyt c and Zn Porph

3.7.1. Calculating the heterogeneous rate constant for Cyt c conjugated to multifunctionalised AuNPs

DPV was performed on 20, 50 and 100 nm AuNP-PEG-Cyt *c*/Zn Porph Ox, AuNP-MUA-Cyt *c*/Zn

Porph Ox Cov and AuNP-MUA-Cyt *c*/Zn Porph Ox Electro (

Figure SI 4). To ensure that the peak current and potential position were as accurate as possible, the

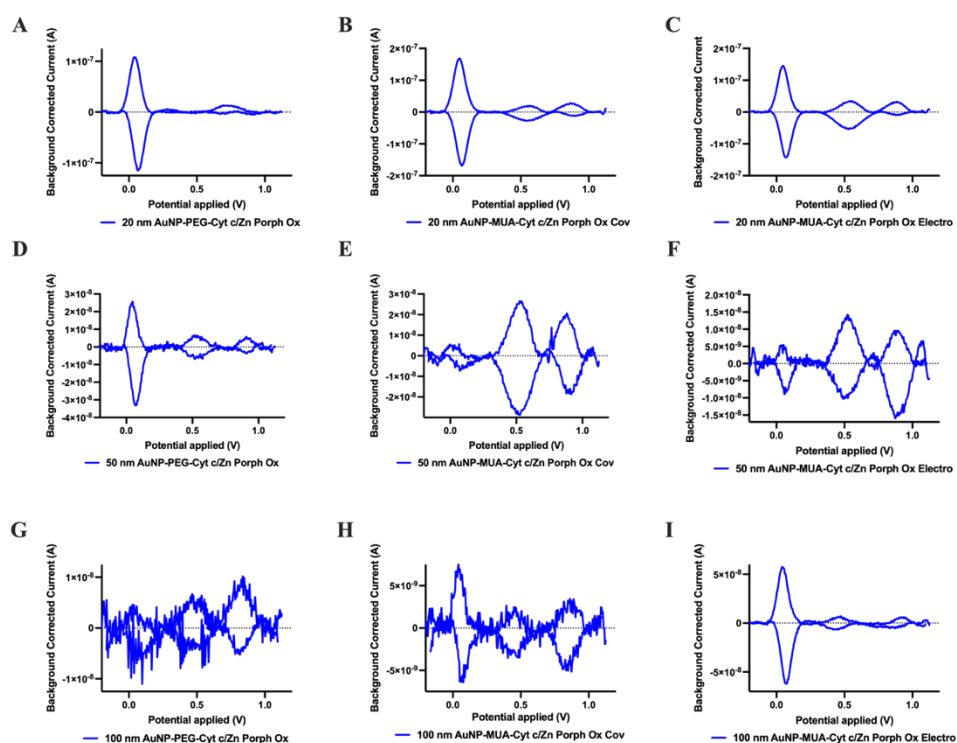DPVs were background subtracted as detailed in 3.6 (Figure 7A-I).

Figure 7. Background corrected typical DPV spectra for the oxidation and reduction peaks for Cyt *c*

and Zn Porph conjugated to 20 , 50 and 100 nm AuNPs with thiol-PEG-carboxyl covalently or MUA

covalently or electrostatically. All DPV displayed were obtained at a scan of 50 mV/s.

Table SI 2 displays the calculated change in potential energy (Δep) for the Cyt *c* that was conjugated

to the multifunctional AuNPs, using the redox peaks from Figure 7A-I. The concentration of the Cyt

c conjugated to AuNPs was normalised to 2 μM via dilution or concentration steps (the concentration

of Cyt *c* and Zn Porph conjugated to AuNPs can be seen in Figure S1). A relationship between the

36

ΔEp and the size of the AuNPs appears to exist, with an increase in ΔEp observed as the size of the AuNPs increases suggesting slower electron transfer kinetics [33], except for the case of 100 nm AuNP-MUA-Cyt c/Zn Porph Ox Electro. This correlation between the size of AuNPs and the ΔEp of Cyt *c* conjugated to them could be the result of the quantity of AuNPs in the samples, as there is an overall greater surface area of Au in the AuNP samples utilising smaller AuNPs. The electron-rich AuNPs may therefore help mediate the reversibility of Cyt *c*, this is supported by work which has shown that AuNPs can act as electrocatalysts [38]. Another perspective is that the correlation between the size of the AuNPs and the ΔEp of Cyt *c* may be due to the number of AuNPs in the sample. The multifunctionalised AuNP samples were normalised for Cyt *c* concentration, and the smaller AuNPs have less Cyt *c* per individual AuNP, therefore, there are more AuNPs in the solution compared to the larger AuNPs and so there is a greater chance of a portion of the AuNPs being surface confined. However, as previously stated, the concertation of analyte at the surface of the electrode is regarded as the bulk concentration [37], so may not influence the ability to determine the kinetics of the electrons moving between the multifunctionalised AuNPs and the electrode.

The heterogeneous rate constants for Cyt *c* conjugated to multifunctionalised AuNPs were calculated from the DPVs of Figure 7A-I, tabulated in Table SI 2 and displayed in Figure 8. The k^0 value of Cyt *c* Red was shown to be lower than that of Cyt *c* Ox, this may be the result of the tertiary structural changes identified in CD in section 3.2

All the multifunctionalised AuNP samples in Figure 8 had a lower k^0 value than Cyt *c* Ox, indicating that the electron transfer rate of Cyt *c* is lower when conjugated to AuNPs, an effect that is likely the result of the change in secondary and tertiary structures, as observed in the CD spectra of Cyt *c*

37

conjugated to AuNPs outlined in section 3.2. The CD spectra of Cyt c conjugated to 20 nm multifunctionalised AuNPs showed the greatest similarity to that of Cyt c Ox free in solution, when compared to 50 and 100 nm multifunctionalsied AuNPs, signalling that the structure of the Cyt c conjugated to the 20 nm multifunctionalised AuNPs was the most comparable to Cyt c Ox free in solution. As a result, the k^0 value of Cyt c conjugated to 20 nm multifunctionalised AuNPs was most comparable to Cyt c Ox.

The Cyt c conjugated to AuNPs using thiol-PEG-carboxyl was hypothesised to have a lower k^0 value than Cyt c conjugated to AuNPs using MUA, due to its proximity to AuNPs and the predicted orientation of Cyt c. However, it appears to only be the proximity of Cyt c to AuNPs that negatively effects the k^0 value, and this influence becomes more significant as the size of AuNPs increases (**Figure SI 5**). Literature suggests that the protein binding constant increases as AuNP size increases, which can cause structural changes to the protein and affect the function [39]. The CD spectra displayed in section 3.2 supports the literature as the Cyt c conjugated to 20 nm AuNPs showed less structural change than the Cyt c conjugated to 50 and 100 nm AuNPs, resulting in higher k^0 values for the 20 nm AuNPs. The higher protein packing density that is observed in larger AuNPs as evidenced in literature, may also be the result of the lower Cyt c k^0 value, as the heme of Cyt c is less accessible when conjugated to 50 and 100 nm AuNPs [39]. The packing density may also explain why the AuNPs functionalised with thiol-PEG-carboxyl showed the highest k^0 values, whereas the k^0 value of AuNPs multifunctionalised using MUA covalently and electrostatically were very similar to each other (Figure SI 5). The longer length of thiol-PEG-carboxyl would result in less conjugated Cyt c per unit of volume when compared to the amount of Cyt c conjugated to MUA, therefore being more accessible to electrons.
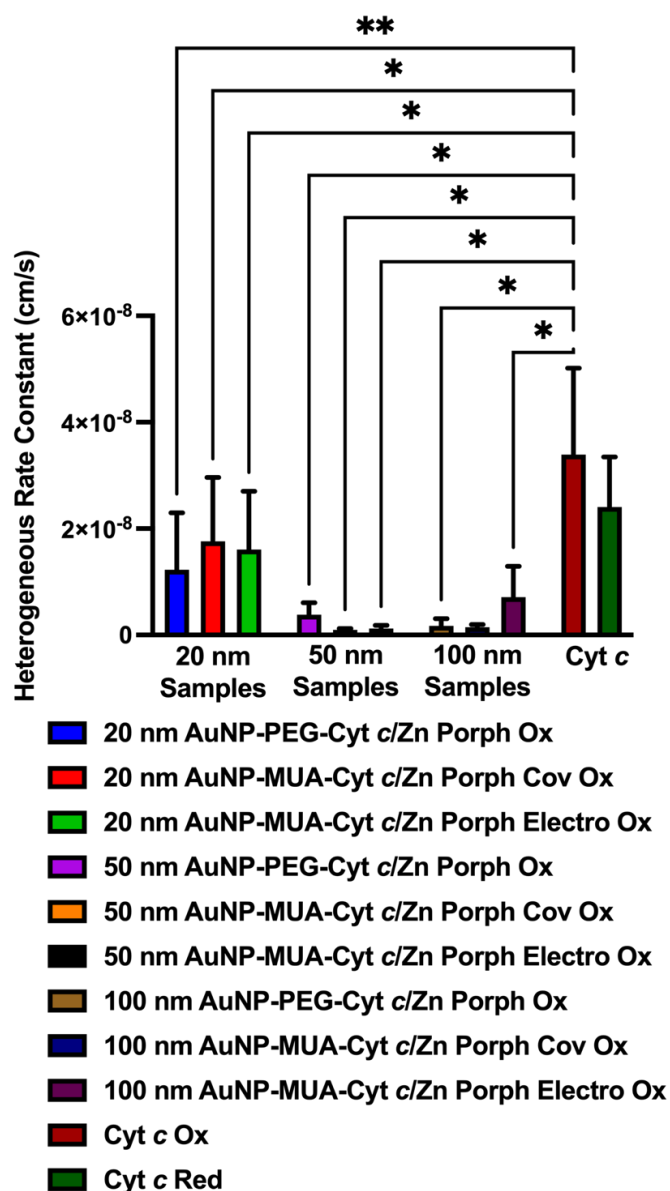
38

Figure 8. Heterogeneous rate constant of Cyt *c* oxidised conjugated to multifunctionalised AuNPs with Zn Porph. AuNPs of 20, 50 and 100 nm were functionalised with different ligands and conjugations methods to determine the effects the components have on the heterogenous rate constant of Cyt *c* when compared to Cyt *c* oxidised free in solution. The statistical analysis was performed using a one-way ANOVA with a post-Dunnett test. Determined by DPV.

39

3.7.2. Calculating the heterogeneous rate constant for Zn Porph conjugated to multifunctionalised AuNPs

The k^0 value of Zn Porph was also essential to determine, and assess the effect, if any, conjugation had upon the electrochemical activity of Zn Porph. A change in electrochemistry may indicate an inability to provide an energy source to Cyt c, which could make the treatment ineffective. The ΔEp showed that, in general, the peak separation of Zn Porph decreased after conjugation to AuNPs, indicating either sample deposition on the ITO electrode or the ability for AuNPs to enhance the reversibility of the Zn Porph. A large ΔEp value was evident for 20 nm AuNP-PEG-Cyt c/Zn Porph Ox, suggesting that the system is electrochemically irreversible [33]. The irreversibility of Zn Porph conjugated to 20 nm AuNP-PEG-Cyt c/Zn Porph Ox could be the result of the Cyt c blocking the accessibility of Zn Porph, resultantly decreasing the kinetics between Zn Porph and the electrode surface.

The k^0 values of Zn Porph were determined by analysing the DPV data with background correction (examples shown in Figure 7A-I and summarised in Table SI 3). The results indicated no significant alteration in the k^0 values of Zn Porph after conjugation to multifunctionalised AuNPs of varying sizes and using different ligands and conjugation methods compared to Zn Porph free in solution (Figure 9). However, the standard deviation (SD) of Zn Porph in solution was relatively large, making it difficult to determine the exact impact of the conjugation to AuNPs. Nonetheless, the mean k^0 values of Zn Porph conjugated to multifunctionalised AuNPs were observed to be lower than the free Zn Porph in solution.

40

The k^0 values of Zn Porph conjugated to AuNPs were statistically compared to each other to identify whether any component significantly affected the electrochemical ability of Zn Porph (Figure SI 6). The results show that the size of AuNPs and the lengths of the linkers most greatly affected the k^0 values of Zn Porph conjugated to AuNPs, as also observed in Cyt c conjugated to AuNPs. The Zn Porph conjugated to 50 and 100 nm AuNPs showed a significant difference from each other, with the mean k^0 values being lowest for Zn Porph conjugated to 100 nm AuNPs. This is presumably the result of higher amounts of Zn Porph and Cyt c bound to each of the larger AuNPs, decreasing the accessibility of each of the conjugated molecules and therefore slowing the rate of electron transfer.
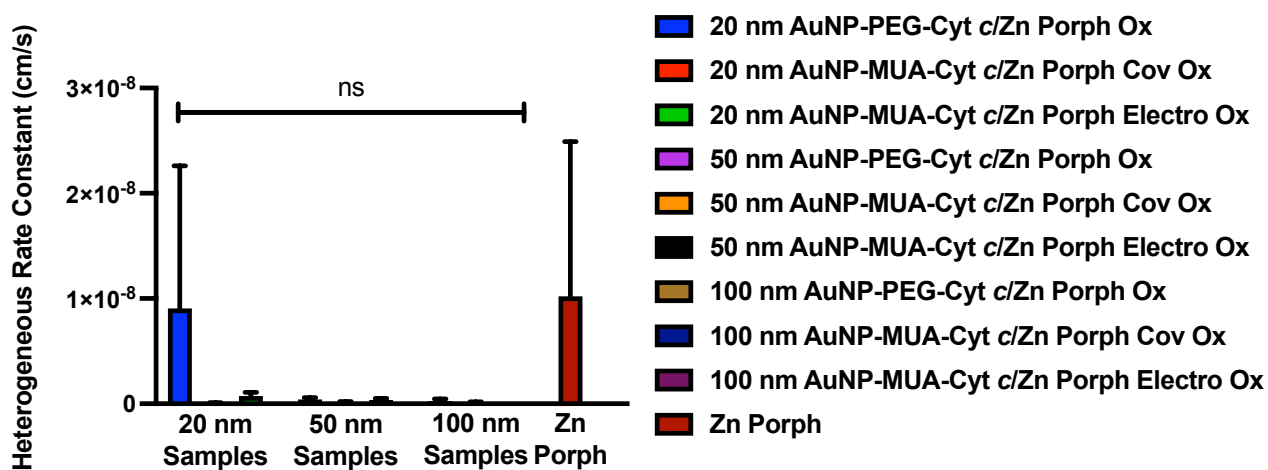

Figure 9. The heterogeneous rate constant was determined from the first redox peak of Zn Porph, located at 0.4-0.7 V free in solution and conjugated to multifunctionalised AuNPs with Cyt c Ox. AuNPs of 20, 50 and 100 nm were functionalised with different ligands and conjugations methods to determine the effects the components have on the heterogenous rate constant of Zn Porph when compared to Zn Porph free in solution. The statistical analysis was performed using a one-way ANOVA with a post-Dunnett test. Determined by DPV.

41

Overall, the calculated k^0 values for Cyt c are lower after conjugation to multifunctionalised AuNPs, the likely result of structural changes observed in the CD spectra. The k^0 values can be correlated to the packing density influenced by the ligand length, as longer ligands would have a lower packing density making the Cyt c more accessible to the electrode surface. The larger AuNPs have been previously shown to conjugate stronger to proteins than smaller AuNPs, which can have a greater effect on the structural change of Cyt c (as observed in the CD) and, therefore its electrochemical ability. The Zn Porph showed no significant change in k^0 value after conjugation to multifunctionalised AuNPs, attributed to the large SD of Zn Porph free in solution. Comparison between the k^0 values of Zn Porph conjugated to differing sizes of multifunctionalised AuNPs concluded that the larger AuNPs reduce the electron transfer ability of Zn Porph due to the higher number of conjugated molecules per AuNP, meaning the molecules are less accessible to electrons.

4. Conclusion

In this work, we examined the electrochemical behaviour of Cyt c and Zn Porph pre- and post-conjugation to AuNPs. We determined that structural modifications in Cyt c, arising from its conjugation to AuNPs, brought about significant alterations in secondary and tertiary structures, with thiol-PEG-carboxyl functionalized AuNPs inducing the least changes. The structural modifications appear to be determined by either the proximity of Cyt c to the AuNP or the packing density. Surprisingly, covalent conjugation methods, which were expected to significantly alter the structure of Cyt c due to stronger bonding, caused less structural change than AuNP-MUA-Cyt c Ox electrostatic conjugation. ToF-SIMS confirmed that the conjugation method did not significantly impact the orientation of Cyt c. Instead, the ligand used in the conjugation process largely dictated

42

this orientation. Higher packing densities were noted on AuNPs using MUA as a ligand due to its shorter length. Post-conjugation, the k^0 values of Cyt c decreased, likely due to structural changes and packing density influenced by ligand length. Conversely, the k^0 values of Zn Porph were largely unaffected. Interestingly, the overall redox abilities of Cyt c and Zn Porph remained consistent post-conjugation to AuNPs, indicating that the function of the protein and the fluorescent molecule was unaffected by the different parameters. This work demonstrates the potential for accurately evaluating protein function in complex nanoparticle systems. Such insights provide a deeper understanding of how various conjugation approaches influence protein functionality, enabling researchers to optimize their formulations.

5. Declaration of Competing Interest

The authors declare that they have no known competing financial interests or personal relationships that could have appeared to influence the work reported in this paper.

6. Acknowledgements

7. Data availability

Data will be made available https://rdmc.nottingham.ac.uk/ doi to be confirmed once accepted for

publications.

8. Declaration of generative AI and AI-assisted technologies in the writing process

During the preparation of this work the author(s) used ChatGPT in order to correct grammar errors and improve the readability fo the text. After using this tool/service, the author(s) reviewed and edited the content as needed and take(s) full responsibility for the content of the publication.

9. References

[1] C. Garrido, L. Galluzzi, M. Brunet, P.E. Puig, C. Didelot, G. Kroemer, Mechanisms of cytochrome c release from mitochondria, Cell Death And Differentiation, 13 (2006) 1423.
[2] J. Cai, J. Yang, D. Jones, Mitochondrial control of apoptosis: the role of cytochrome c, Biochimica et Biophysica Acta (BBA) - Bioenergetics, 1366 (1998) 139-149.
[3] M. Weller, T. Overton, J. Rourke, F. Armstrong, Inorganic Chemistry, OUP Oxford2014.
[4] D.G.G. McMillan, S.J. Marritt, M.A. Firer-Sherwood, L. Shi, D.J. Richardson, S.D. Evans, S.J. Elliott, J.N. Butt, L.J.C. Jeuken, Protein–Protein Interaction Regulates the Direction of Catalysis and Electron Transfer in a Redox Enzyme Complex, Journal of the American Chemical Society, 135 (2013) 10550-10556.
[5] Y. Liu, J.K. Fredrickson, N.C. Sadler, P. Nandhikonda, R.D. Smith, A.T. Wright, Advancing understanding of microbial bioenergy conversion processes by activity-based protein profiling, Biotechnology for Biofuels, 8 (2015) 156.
[6] Y. Wu, S. Hu, Biosensors based on direct electron transfer in redox proteins, Microchimica Acta, 159 (2007) 1-17.
[7] J. Pessoa, Cytochrome c in cancer therapy and prognosis, Bioscience Reports, 42 (2022).
[8] G. Gilardi, A. Fantuzzi, Manipulating redox systems: application to nanotechnology, TRENDS in Biotechnology, 19 (2001) 468-476.
[9] A.F.A.A. Melo, G.C. Sedenho, I. Osica, K. Ariga, F.N. Crespilho, Electrochemical Behavior of Cytochrome C Immobilized in a Magnetically Induced Mesoporous Framework, ChemElectroChem, 6 (2019) 5802-5809.
[10] W. Al-Shakarchi, A. Alsuraifi, M. Abed, M. Abdullah, A. Richardson, A. Curtis, C. Hoskins, Combined Effect of Anticancer Agents and Cytochrome C Decorated Hybrid Nanoparticles for Liver Cancer Therapy, Pharmaceutics, 10 (2018) 48.
[11] W. Al-Shakarchi, A. Alsuraifi, A. Curtis, C. Hoskins, Dual Acting Polymeric Nano-Aggregates for Liver Cancer Therapy, Pharmaceutics, 10 (2018).
[12] W. Shang, J.H. Nuffer, V.A. Muñiz-Papandrea, W. Colón, R.W. Siegel, J.S. Dordick, Cytochrome C on silica nanoparticles: influence of nanoparticle size on protein structure, stability, and activity, Small, 5 (2009) 470-476.
[13] C. Guo, J. Wang, X. Chen, Y. Li, L. Wu, J. Zhang, C.-a. Tao, Construction of a Biosensor Based on a Combination of Cytochrome c, Graphene, and Gold Nanoparticles, Sensors, 19 (2018).
[14] E.J. Tollefson, C.R. Allen, G. Chong, X. Zhang, N.D. Rozanov, A. Bautista, J.J. Cerda, J.A. Pedersen, C.J. Murphy, E.E. Carlson, R. Hernandez, Preferential Binding of Cytochrome c to Anionic Ligand-Coated Gold Nanoparticles: A Complementary Computational and Experimental Approach, ACS Nano, 13 (2019) 6856-6866.
[15] W. Haiss, N.T.K. Thanh, J. Aveyard, D.G. Fernig, Determination of Size and Concentration of Gold Nanoparticles from UV–Vis Spectra, Analytical Chemistry, 79 (2007) 4215-4221.

[16] V. Amendola, R. Pilot, M. Frasconi, O.M. Maragò, M.A. Iatì, Surface plasmon resonance in gold nanoparticles: a review, Journal of Physics: Condensed Matter, 29 (2017) 203002.

[17] E. Romanovskaia, P. Slovenský, S.M. Kalantarian, L. Laundry-Mottiar, V. Romanovski, M. Halama, M. Auinger, Y.S. Hedberg, Electrochemical Estimations of the Gold Nanoparticle Size Effect on Cysteine-Gold Oxidation, Journal of The Electrochemical Society, 169 (2022) 021501.

[18] A. Barfidokht, S. Ciampi, E. Luais, N. Darwish, J.J. Gooding, Distance-Dependent Electron Transfer at Passivated Electrodes Decorated by Gold Nanoparticles, Analytical Chemistry, 85 (2013) 1073-1080.

[19] A. Jain, G.F. Trindade, J.M. Hicks, J.C. Potts, R. Rahman, R.J.M. Hague, D.B. Amabilino, L. Pérez-García, F.J. Rawson, Modulating the biological function of protein by tailoring the adsorption orientation on nanoparticles, Journal of Colloid and Interface Science, 587 (2021) 150-161.

[20] J.E. Baio, T. Weidner, D. Ramey, L. Pruzinsky, D.G. Castner, Probing the orientation of electrostatically immobilized cytochrome C by time of flight secondary ion mass spectrometry and sum frequency generation spectroscopy, Biointerphases, 8 (2013) 18.

[21] A. Jain, J. Gosling, S. Liu, H. Wang, E.M. Stone, S. Chakraborty, P.-S. Jayaraman, S. Smith, D.B. Amabilino, M. Fromhold, Y.-T. Long, L. Pérez-García, L. Turyanska, R. Rahman, F.J. Rawson, Wireless electrical–molecular quantum signalling for cancer cell apoptosis, Nature Nanotechnology, (2023).

[22] J.C. Potts, A. Jain, D.B. Amabilino, F.J. Rawson, L. Pérez-García, Molecular Surface Quantification of Multifunctionalized Gold Nanoparticles Using UV–Visible Absorption Spectroscopy Deconvolution, Analytical Chemistry, (2023).

[23] N.J. Greenfield, Using circular dichroism spectra to estimate protein secondary structure, Nat Protoc, 1 (2006) 2876-2890.

[24] S. Vinogradov, R. Zand, Circular dichroism studies: I. Cytochrome c, Archives of biochemistry and biophysics, 125 (1968) 902-910.

[25] M. Biedulska, P. Jakóbczyk, M. Sosnowska, B. Dec, A. Muchlińska, A.J. Zaczek, D. Nidzworski, R. Bogdanowicz, Cytocompatibility of stabilized black phosphorus nanosheets tailored by directly conjugated polymeric micelles for human breast cancer therapy, Scientific Reports, 11 (2021) 9304.

[26] A.K. Yagati, T. Lee, J. Min, J.-W. Choi, Electrochemical performance of gold nanoparticle–cytochrome c hybrid interface for H2O2 detection, Colloids and Surfaces B: Biointerfaces, 92 (2012) 161-167.

[27] X. Chen, R. Ferrigno, J. Yang, G.M. Whitesides, Redox Properties of Cytochrome c Adsorbed on Self-Assembled Monolayers: A Probe for Protein Conformation and Orientation, Langmuir, 18 (2002) 7009-7015.

[28] A. Molina, E. Laborda, F. Martínez-Ortiz, D.F. Bradley, D.J. Schiffrin, R.G. Compton, Comparison between double pulse and multipulse differential techniques, 659 (2011) 12-24.

[29] D.T. Miles, R.W. Murray, Temperature-Dependent Quantized Double Layer Charging of Monolayer-Protected Gold Clusters, Analytical Chemistry, 75 (2003) 1251-1257.

[30] A.J. Bard, L.R. Faulkner, Electrochemical Methods: Fundamentals and Applicaitons, 2e Student Solutions Manual, Wiley2002.

[31] J.M. Hicks, Z.Y. Wong, D.J. Scurr, N. Silman, S.K. Jackson, P.M. Mendes, J.W. Aylott, F.J. Rawson, Tailoring the Electrochemical Properties of Carbon Nanotube

Modified Indium Tin Oxide via in Situ Grafting of Aryl Diazonium, Langmuir, 33 (2017) 4924-4933.

[32] I. Lavagnini, R. Antiochia, F. Magno, An Extended Method for the Practical Evaluation of the Standard Rate Constant from Cyclic Voltammetric Data, Electroanalysis, 16 (2004) 505-506.

[33] N. Elgrishi, K.J. Rountree, B.D. McCarthy, E.S. Rountree, T.T. Eisenhart, J.L. Dempsey, A Practical Beginner's Guide to Cyclic Voltammetry, Journal of Chemical Education, 95 (2018) 197-206.

[34] H. Liu, H. Yamamoto, J. Wei, D.H. Waldeck, Control of the Electron Transfer Rate between Cytochrome c and Gold Electrodes by the Manipulation of the Electrode's Hydrogen Bonding Character, Langmuir, 19 (2003) 2378-2387.

[35] A.L. Eckermann, D.J. Feld, J.A. Shaw, T.J. Meade, Electrochemistry of redox-active self-assembled monolayers, Coord Chem Rev, 254 (2010) 1769-1802.

[36] P. Kalimuthu, M.D. Heath, J.M. Santini, U. Kappler, P.V. Bernhardt, Electrochemically driven catalysis of Rhizobium sp. NT-26 arsenite oxidase with its native electron acceptor cytochrome c552, Biochimica et Biophysica Acta (BBA) - Bioenergetics, 1837 (2014) 112-120.

[37] A.J. Bard, L.R. Faulkner, H.S. White, Electrochemical Methods: Fundamentals and Applications, Wiley2022.

[38] C. Li, O.J.H. Chai, Q. Yao, Z. Liu, L. Wang, H. Wang, J. Xie, Electrocatalysis of gold-based nanoparticles and nanoclusters, Materials Horizons, 8 (2021) 1657-1682.

[39] S.H.D.P. Lacerda, J.J. Park, C. Meuse, D. Pristinski, M.L. Becker, A. Karim, J.F. Douglas, Interaction of Gold Nanoparticles with Common Human Blood Proteins, ACS Nano, 4 (2010) 365-379.

Supporting Information:

Electrochemical Analysis of Gold Nanoparticles Multifunctionalised with Cytochrome c

and a Zinc Porphyrin

Jordan C. Potts[a], Akhil Jain[b], David B. Amabilino[c], Lluïsa Pérez-García[a,d,e] and Frankie J.

Rawson[b]*

[a] Division of Advanced Materials and Healthcare Technologies, School of Pharmacy, University of

Nottingham, Nottingham NG7 2RD, UK

[b] Bioelectronics Laboratory, Division of Regenerative Medicine and Cellular Therapies, School of

Pharmacy, University of Nottingham, Biodiscovery Institute, Nottingham NG7 2RD, UK

[c] Institut de Ciència de Materials de Barcelona (ICMAB), CSIC, Carrer dels Til·lers, Campus

Universitari, 08193 Cerdanyola del Vallès, Catalunya, Spain

[d] Departament de Farmacologia, Toxicologia i Química Terapèutica, Facultat de Farmàcia i

Ciències de l'Alimentació, Universitat de Barcelona, 08028 Barcelona, Catalunya, Spain

[e] Institut de Nanociència i Nanotecnologia UB (IN2UB), Universitat de Barcelona, 08028 Barcelona,
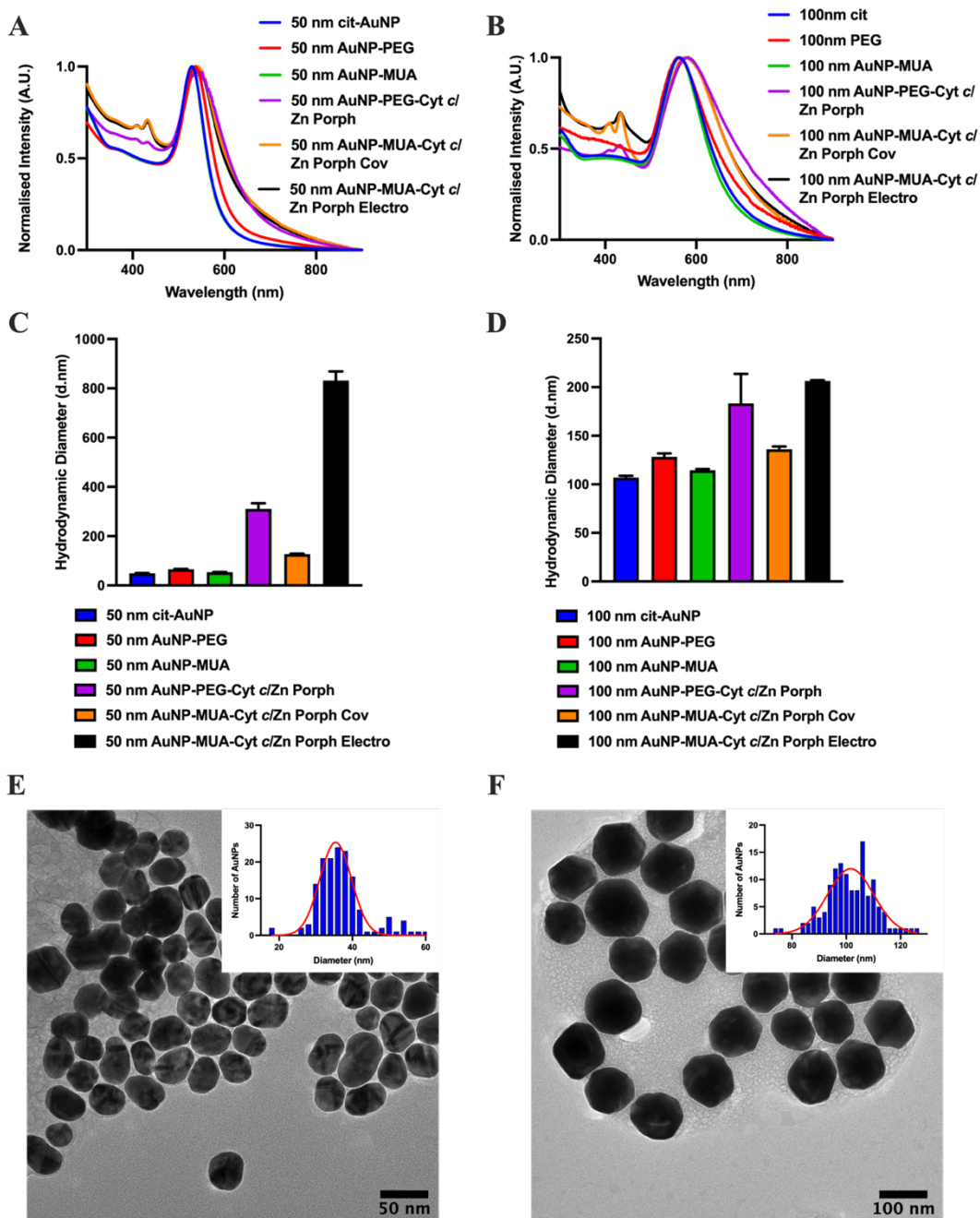Catalunya, Spain

Figure SI 1. The physicochemical characterisation of multifunctionalised AuNPs using UV-Vis absorption spectroscopy for 50 nm AuNPS (A), 100 nm AuNPs (B) and using DLS for 50 nm AuNPs (C) and 100 nm AuNPs (D). TEM images for 50 nm AuNP-PEG-Cyt *c*/Zn Porph (E) and 100 nm AuNP-PEG-Cyt *c*/Zn Porph (F) with a cumulative frequency distribution included in the insert made using 163, 50 nm AuNPs and 128, AuNPs 100 nm AuNPs.

```python
import math

def calculate_D(delta_i_max, n, F, A, C, delta_tau, R, T, delta_E):
    """
    Calculate the diffusion coefficient D using the provided equation.

    Parameters:
    delta_i_max (float): Maximum change in current
    n (float): Number of electrons transferred
    F (float): Faraday constant (96485 C/mol)
    A (float): Electrode surface area
    C (float): Concentration
    delta_tau (float): Time interval
    R (float): Universal gas constant (8.314 J/(mol·K))
    T (float): Temperature in Kelvin
    delta_E (float): Potential difference

    Returns:
    float: Diffusion coefficient D or None if the calculation is not valid
    """

    sigma = math.exp(n * F / (R * T) * delta_E / 2)
    term_inside_sqrt = (1 - sigma) / (1 + sigma)

    if term_inside_sqrt < 0:
        print("Error: The term inside the square root is negative. Check input values.")
        return None

    prefactor = n * F * A * C * math.sqrt(1 / (math.pi * delta_tau) * term_inside_sqrt)
    D = (delta_i_max / prefactor) ** 2

    return D

# Example Usage:
F = 96485  # C/mol
R = 8.314  # J/(mol·K)
# Example values for other parameters (please replace with actual values)
n = 1
A = 38.38
C = 2e-6
delta_tau = 0.05
T = 295.15
delta_E = -0.05
delta_i_max = -6.42E-09

D_value = calculate_D(delta_i_max, n, F, A, C, delta_tau, R, T, delta_E)
if D_value:
    print(f"Diffusion coefficient D = {D_value} cm^2/s")
```

Figure SI 2: Python code calculator used to determine the diffusion coefficient for analytes when using DPV.

This was necessary due to the complex shape of the voltammogram. DPV experiments were conducted on PBS (25 mM) and AuNPs, which did not show significant peaks. Therefore, any deviations from the DPV shape of PBS and AuNPs were attributed to the conjugated molecules. The DPVs were plotted in OriginPro (2018) (Figure SI 3A) and peak analysis was performed by selecting the "Peak Analyzer" from the "Analysis" tab. "Subtract Baseline" and "User-Defined Baseline Mode" were selected, and the 1st and 2nd derivatives were chosen as the methods for finding anchor points. Adjacent-averaging smoothing was used with a window size of 3, threshold of 0.05, and 8 anchor points were selected. The software automatically placed anchor points on the voltammogram, and minor adjustments were made to ensure that each anchor point was positioned before and after the regions of interest. Once the anchor points were in the correct position, the interpolation method "Spline" was selected to create a smooth curve fitting the shape of the voltammograms. The "Finish" button was then selected on the peak analyser (Figure SI 3B). The background-subtracted voltammogram was plotted, and the "Quick Peaks" option was selected from the "Gadgets" section. The region of interest box (ROI) was positioned over the peak, and if found, the peak height and position were output into a table. This method was conducted for each sample at scan rates of 50 mV/s, 25 mV/s, and 10 mV/s for both the oxidation and reduction peaks to obtain the most accurate measurements.
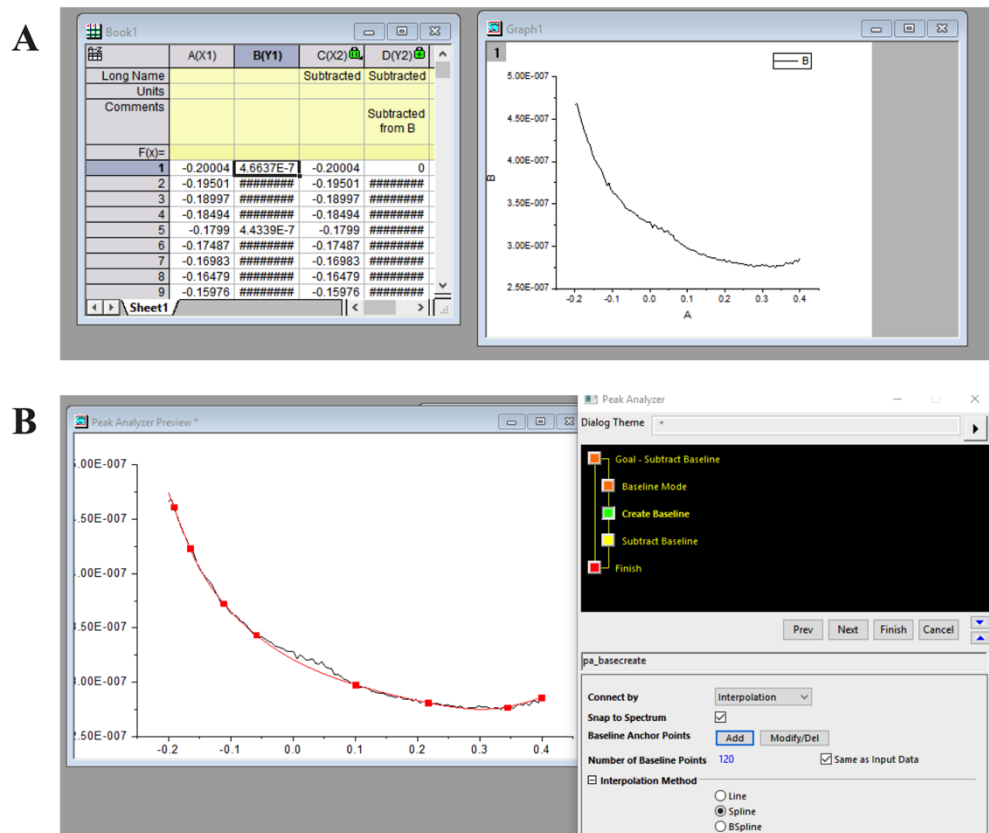
Figure SI 3. How DPV oxidation and reduction peaks were analysed in OriginPro (2018). The DPV was first plotted in OriginPro (A), the peak analyser was then selected to make a 4th order polynomial background to fit the DPV trace using 8 nodes with a spline interpolation method selected (B).

Table SI 1: Concentration of Cyt *c* oxidised and Zn Porph bound to multifunctionalised AuNPs of various sizes and conjugated using different mechanisms, were determined. The concentration of Cyt *c* was normalised in the samples to 2 mM.

| Sample	Average Concentration of Cyt *c* (mM)	Average Concentration of Zn Porph (mM)
20 nm AuNP-PEG-Cyt c/Zn Porph Ox	2	1.47
20 nm AuNP-MUA-Cyt c/Zn Porph Cov Ox	2	23.3
20 nm AuNP-MUA-Cyt c/Zn Porph Ox Electro	2	5.56
50 nm AuNP-PEG-Cyt c/Zn Porph Ox	2	3.21
50 nm AuNP-MUA-Cyt c/Zn Porph Ox Cov	2	17.36
50 nm AuNP-MUA-Cyt c/Zn Porph Ox Electro	2	2.29
100 nm AuNP-PEG-Cyt c/Zn Porph Ox	2	5.04
100 nm AuNP-MUA-Cyt c/Zn Porph Cov Ox	2	7.94
100 nm AuNP-MUA-Cyt c/Zn Porph Ox Electro	2	31.80
Cyt *c*	2	-
Zn Porph	-	2
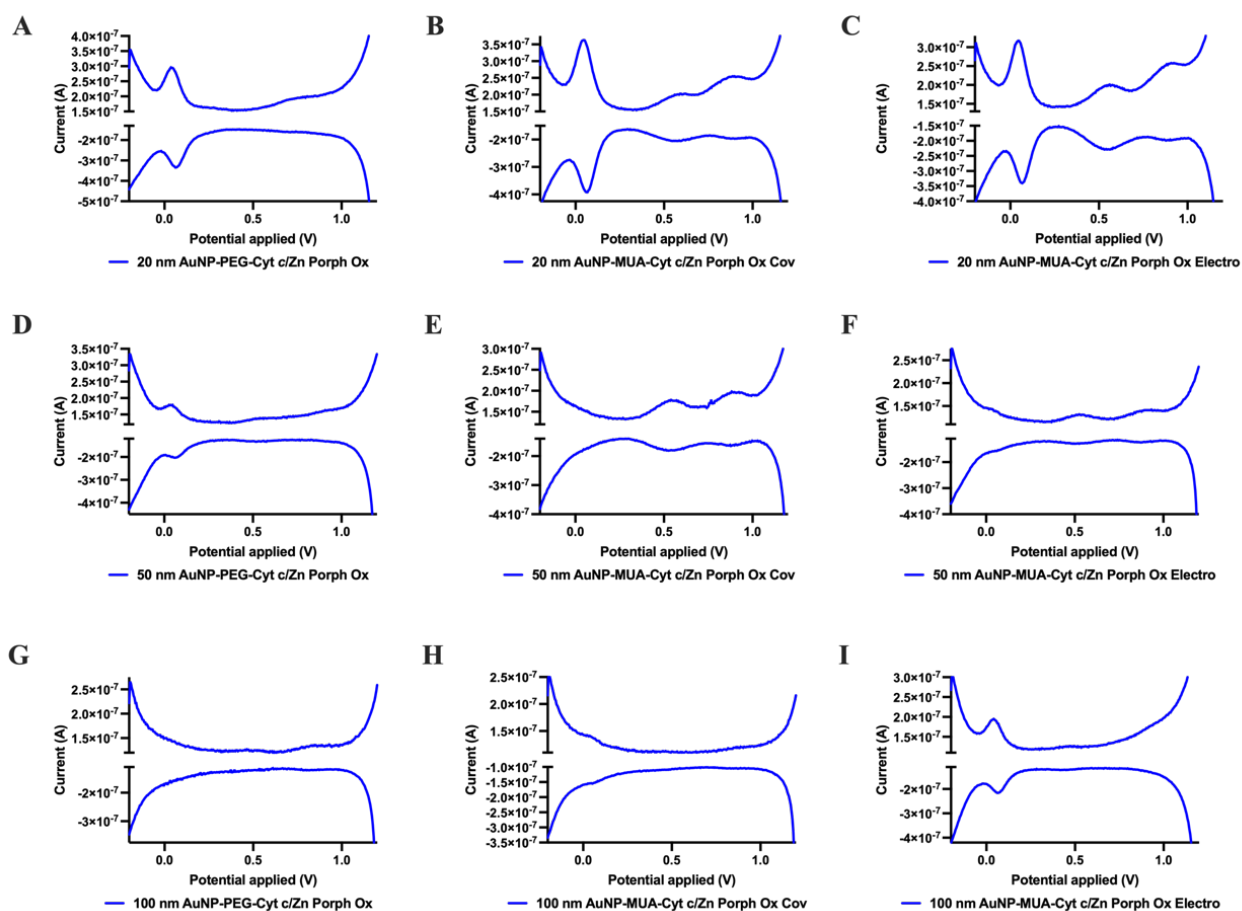
Figure SI 4. DPV of 20, 50 and 100 nm AuNPs multifucntionalised with Cyt *c* and Zn Porph using thiol-PEG-carboxyl covalently and MUA covalently and electrostatically. 20 nm AuNP-PEG-Cyt *c*/Zn Porph Ox (A), 20 nm AuNP-MUA-Cyt *c*/Zn Porph Ox Cov (B), 20 nm AuNP-MUA-Cyt *c*/Zn Porph Ox Electro (C), 50 nm AuNP-PEG-Cyt *c*/Zn Porph Ox (D), 50 nm AuNP-MUA-Cyt *c*/Zn Porph Ox Cov (E), 50 nm AuNP-MUA-Cyt *c*/Zn Porph Ox Electro (F), 100 nm AuNP-PEG-Cyt *c*/Zn Porph Ox (G), 100 nm AuNP-MUA-Cyt *c*/Zn Porph Ox Cov (H) and 20 nm AuNP-MUA-Cyt *c*/Zn Porph Ox Electro (I).

Table SI 2 : DPV was used to identify the oxidation peak to reduction peak and heterogeneous rate constant of Cyt *c* oxidised bound to multifunctionalised AuNPs of various sizes and conjugated using different mechanisms.

Sample	ΔEp (mV)	Mean Heterogeneous Rate Constant (k^0) (cm/s)
20 nm AuNP-PEG-Cyt c/Zn Porph Ox	23.66	$1.23 \times 10^{-8} \pm 1.07 \times 10^{-8}$
20 nm AuNP-MUA-Cyt c/Zn Porph Cov Ox	11.9	$1.76 \times 10^{-8} \pm 1.20 \times 10^{-8}$
20 nm AuNP-MUA-Cyt c/Zn Porph Ox		$1.61 \times 10^{-8} \pm 1.10 \times 10^{-8}$
Electro	21.98	
50 nm AuNP-PEG-Cyt c/Zn Porph Ox	25.32	$3.76 \times 10^{-9} \pm 2.27 \times 10^{-9}$
50 nm AuNP-MUA-Cyt c/Zn Porph Ox Cov	28.70	$9.70 \times 10^{-10} \pm 2.74 \times 10^{-10}$
50 nm AuNP-MUA-Cyt c/Zn Porph Ox		$1.25 \times 10^{-9} \pm 6.00 \times 10^{-10}$
Electro	32.04	
100 nm AuNP-PEG-Cyt c/Zn Porph Ox	40.44	$1.71 \times 10^{-9} \pm 1.36 \times 10^{-9}$
100 nm AuNP-MUA-Cyt c/Zn Porph Cov Ox	42.93	$1.45 \times 10^{-9} \pm 5.42 \times 10^{-10}$
100 nm AuNP-MUA-Cyt c/Zn Porph Ox		$7.14 \times 10^{-9} \pm 5.79 \times 10^{-10}$
Electro	23.62	
Cyt *c* Ox	18.61	$3.39 \times 10^{-8} \pm 1.63 \times 10^{-8}$
Cyt *c* Red	27.03	$2.41 \times 10^{-8} \pm 9.39 \times 10^{-8}$

Table SI 3. DPV was used to identify the oxidation peak to reduction peak and heterogeneous rate constant of Zn Porph oxidised bound to multifunctionalised AuNPs of various sizes and conjugated using different mechanisms,.

| Sample	ΔEp (mV)	Mean Heterogeneous Rate Constant (k^0) (cm/s)
20 nm AuNP-PEG-Cyt c/Zn Porph Ox	265.30	$3.02 \times 10^{-3} \pm 3.28 \times 10^{-3}$
20 nm AuNP-MUA-Cyt c/Zn Porph Cov Ox	28.40	$1.37 \times 10^{-3} \pm 7.11 \times 10^{-4}$
20 nm AuNP-MUA-Cyt c/Zn Porph Ox Electro	9.90	$7.55 \times 10^{-4} \pm 3.90 \times 10^{-4}$
50 nm AuNP-PEG-Cyt c/Zn Porph Ox	25.30	$3.14 \times 10^{-4} \pm 1.33 \times 10^{-4}$
50 nm AuNP-MUA-Cyt c/Zn Porph Ox Cov	20.00	$1.19 \times 10^{-4} \pm 3.50 \times 10^{-5}$
50 nm AuNP-MUA-Cyt c/Zn Porph Ox Electro	45.20	$3.27 \times 10^{-4} \pm 6.77 \times 10^{-5}$
100 nm AuNP-PEG-Cyt c/Zn Porph Ox	8.50	$1.80 \times 10^{-4} \pm 1.50 \times 10^{-4}$
100 nm AuNP-MUA-Cyt c/Zn Porph Cov Ox	22.80	$8.61 \times 10^{-5} \pm 5.98 \times 10^{-5}$
100 nm AuNP-MUA-Cyt c/Zn Porph Ox Electro	36.80	$1.43 \times 10^{-5} \pm 4.61 \times 10^{-6}$
Zn Porph	55.50	$3.38 \times 10^{-3} \pm 4.07 \times 10^{-3}$
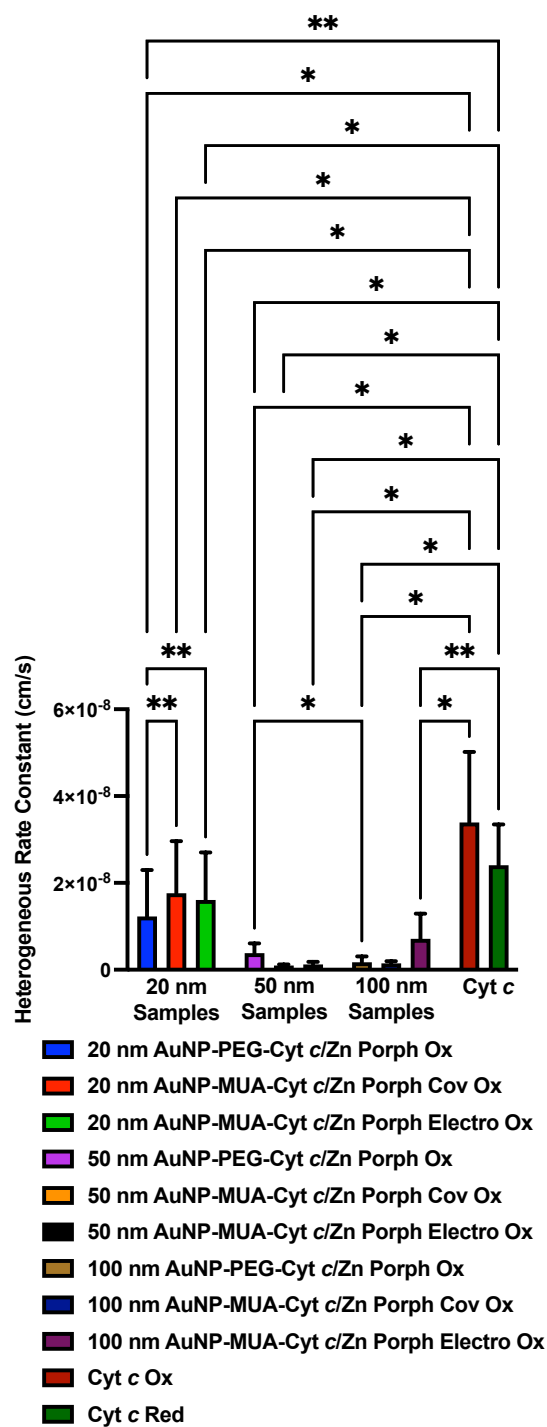
Figure SI 5. Heterogenous rate constant (k^0) of Cyt c oxidised conjugated to multifunctionalised AuNPs with Zn Porph. AuNPs of 20, 50 and 100 nm were functionalised with different ligands and conjugations methods. The k^0 values were compared to each other using a one-way ANOVA with a post-Tukey test. Determined by DPV.
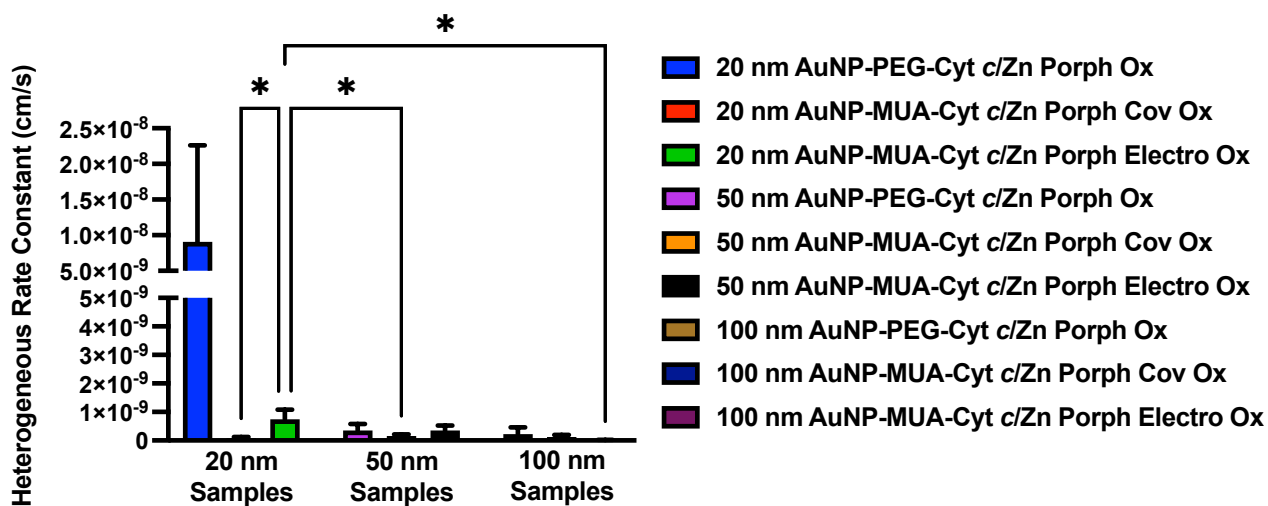
Figure SI 6. Heterogenous rate constant (k^0) of Zn Porph conjugated to multifunctionalised AuNPs with Zn Porph. AuNPs of 20, 50 and 100 nm were functionalised with different ligands and conjugations methods. The k^0 values were compared to each other using a one-way ANOVA with a post-Tukey test . Determined by DPV.